Global and Planetary Change 210 (2022) 103775

Contents lists available at ScienceDirect

Global and Planetary Change

journal homepage: www.elsevier.com/locate/gloplacha

High-frequency sea-level analysis: Global distributions

Petra Zemunik [a,*], Cléa Denamiel [b], Jadranka Šepić [c], Ivica Vilibić [a,b]

[a] Institute of Oceanography and Fisheries, Šetalište I. Meštrovića 63, 21000 Split, Croatia
[b] Ruđer Bošković Institute, Division for Marine and Environmental Research, Bijenička cesta 54, 10000 Zagreb, Croatia
[c] Faculty of Science, University of Split, R. Boškovića 33, 21000 Split, Croatia

ARTICLE INFO

Keywords:
High-frequency sea level
Tide-gauge records
Atmosphere-ocean interaction
Meteotsunami

ABSTRACT

This paper provides global climatology of high-frequency ($T < 2$ h) sea-level oscillations of atmospheric origin. Sea-level series with a temporal resolution of 1 min from 331 tide gauges in the world ocean and spanning between 1.5 and 12 years were analysed to determine the typical ranges, seasons and characteristics of moderate and extreme manifestations of nonseismic sea-level oscillations at tsunami timescales (NSLOTTs). Variances in these oscillations reach 6.6 cm^2 on average, but their region-averaged extreme (99.99th percentile) ranges may exceed half a metre or more at individual hotspot locations. The NSLOTTs are the highest in the mid-latitudes and decrease towards polar and tropical regions. Moderate oscillations show clear winter maxima at the majority of stations, while a less pronounced pattern is evident for the most extreme oscillations, which may occur throughout a year. A total of 3080 of the most prominent NSLOTT events were selected from 308 stations and compared to background oscillations, revealing the substantial capability of energy amplification during extreme events. Synchronicity in extreme NSLOTT events between neighbouring stations (up to 250 km) in mid-latitudes has been detected for 20–32% of all episodes, suggesting possible connectivity between the episodes.

1. Introduction

Atmospherically induced extreme sea levels associated with flooding, which may produce substantial damage to coastal urban areas, are major coastal ocean hazards along with seismic and landslide tsunamis (Nicholls, 2011; Neumann et al., 2015). Additionally, the impact on the coastal hazards of climate change and accelerated sea-level rise i.e., the increase in the magnitude and incidence of extreme sea levels (Douglas, 1992; Church and White, 2006; Cayan et al., 2008; Woodworth et al., 2011), has been at the forefront of sea-level research (Hunter, 2010; Arns et al., 2013; Calafat and Marcos, 2020). Consequently, research and literature on atmospherically driven sea-level extremes, such as surges induced by hurricanes, typhoons and wave storms under both historical and climate warming conditions, are constantly growing (Camelo et al., 2020).

However, due to a lack of available global or regional continuous and long-term sea-level data on a minute timescale, systematic research and climatologies of nonseismic sea-level oscillations on tsunami timescales (NSLOTTs, Vilibić and Šepić, 2017) and of their extreme manifestations, which are known as meteorological tsunamis (commonly referred to as meteotsunamis), have not been constructed until recently (Bechle et al., 2016; Dusek et al., 2019; Williams et al., 2021a). Meteotsunamis, which tend to act locally on small spatial scales (10–100 km), are intense sea-level oscillations that occur on the tsunami frequency band and are generated by various atmospheric forcings (atmospheric gravity waves, pressure jumps, strong winds, squalls, frontal passages, etc.) (Monserrat et al., 2006; Rabinovich, 2020). Historically, NSLOTT and meteotsunami observational research started with a few event-driven studies in areas prone to meteotsunamis, but this research has been noticeably extended and accelerated in recent decades (Vilibić et al., 2021a). Extensive worldwide NSLOTT and meteotsunami literature can now be found for the local (Hibiya and Kajiura, 1982; Candela et al., 1999; Jansa et al., 2007; Goring, 2009), regional (Šepić et al., 2015a; Pattiaratchi and Wijeratne, 2015; Dusek et al., 2019; Williams et al., 2021a) and global (Vilibić and Šepić, 2017; Rabinovich, 2020; Gusiakov, 2021) scales.

Genesis of meteotsunamis, and therefore of NSLOTTs, is a complex and multiresonant phenomenon that may lead to destructive events that surpass several metres at some locations, such as the Balearic Islands (Monserrat et al., 1991; Gomis et al., 1993; Jansà and Ramis, 2021), the Adriatic Sea (Vilibić and Šepić, 2009; Orlić et al., 2010), the Strait of Sicily (Candela et al., 1999), the Japanese western coastline (Hibiya and

* Corresponding author.
E-mail address: zemunik@izor.hr (P. Zemunik).

https://doi.org/10.1016/j.gloplacha.2022.103775
Received 13 July 2021; Received in revised form 16 February 2022; Accepted 18 February 2022
Available online 21 February 2022

Kajiura, 1982), the Korean eastern coastline (Kim et al., 2021), the Australian western coastline (Pattiaratchi and Wijeratne, 2014, 2015), the US east coast (Dusek et al., 2019), the Great Lakes (Bechle et al., 2016) and many others. Intense atmospheric disturbances travel over the open sea and create waves that are further resonantly amplified when approaching the coastline. Therefore, meteotsunami research encompasses (i) the generation of meteotsunamigenic atmospheric disturbances, (ii) energy transfer towards the sea and (iii) nearshore wave amplification.

Recently, NSLOTT research has been a prerequisite for both hazard assessments and probabilistic estimates of extreme sea levels (Hunter et al., 2017; Vousdoukas et al., 2018; Calafat and Marcos, 2020). In fact, the first NSLOTT global investigation by Vilibić and Šepić (2017) demonstrated the importance of high-frequency oscillations in assessing the overall sea-level budget and showed that the NSLOTT could contribute up to 50% of the sea-level heights in low tidal basins. Furthermore, along the western Australian coast, the percentage of this contribution has increased to 85% of the residual sea-level heights (Pattiaratchi and Wijeratne, 2014). Consequently, the NSLOTT might make a substantial difference when included in the assessment of sea-level extremes. In line with that, Tsimplis et al. (2009) showed that the 50-year sea-level return period might be underestimated up to 40 cm when hourly data are used instead of 5-min records. It is likely that the underestimation might be even larger if considering the NSLOTT processes that occur at a minute timescale (such as infragravity waves, Webb et al., 1991), pointing to the necessity of minute sea-level measurements for the proper assessment of sea-level extremes in the world's oceans.

Despite the growing availability of global datasets providing tide-gauge observations with 1-h resolution, only two global sources with higher sampling frequencies ($\leq$5 min) can currently be used to investigate the NSLOTT and meteotsunamis: (i) the IOC Sea-level Station Monitoring Facility (SLSMF) and (ii) the Minute Sea-Level Analysis (MISELA) dataset. The IOC SLSMF (http://www.ioc-sealevelmonitoring.org/) was established in 2006 following the 2004 Sumatra-Andaman tsunami (Titov et al., 2005) and contains global real-time raw sea-level observations intended for operational use. The MISELA dataset (Zemunik et al., 2021a) was created recently and provides quality checked high-pass ($T < 2$ h) filtered sea-level time series for the period from 2004 to 2019; this dataset is thus appropriate for research purposes. Sea-level data at a minute timescale are also available for some stations in the GESLA dataset (Global Extreme Sea Level Analysis, Woodworth et al., 2016, 2017) or can be obtained for some countries directly from national oceanographic agencies (e.g., NOAA Tides and Currents in the USA, https://tidesandcurrents.noaa.gov; Puertos del Estado in Spain, http://www.puertos.es/en-us/oceanografia/Pages/portus.aspx; Fisheries and Oceans Canada, https://www.waterlevels.gc.ca/eng, the Institute of Oceanography and Fisheries in Croatia, http://faust.izor.hr/autodatapub/postaje, and others).

Several NSLOTT questions remain unanswered: (i) in which regions of the world ocean do they occur most often and with the strongest intensity? (ii) Do they occur preferentially in particular seasons or months? (iii) Do they have common features in some regions or across the globe? (iv) Do they occur simultaneously at nearby locations? Some regional studies have given different answers to these questions. For example, Williams et al. (2021a) claim that most meteotsunamis in northwestern Europe occur in winter, yet at other locations, summer maxima are predominant (e.g., Orlić (2015) for the Adriatic Sea; Bechle et al. (2016) for the US Great Lakes). However, the methodology between these studies is quite different; some of them are based on eyewitness cataloguing, while others are based on multiyear high-frequency sea-level observations. Additionally, many locations (e.g., the Adriatic Sea, Orlić (2015); Ciutadella, Jansà and Ramis (2021); the Great Lakes, Bechle et al. (2016); and the southern coast of Sicily, Zemunik et al. (2021c)) are known as meteotsunami hotspots, but it is likely that there are more hotspots at more isolated locations that have been missed by eyewitnesses and/or not captured by tide-gauge records. Furthermore, in 2014, a chain of destructive meteorological tsunamis over the Mediterranean and Black Seas was documented (Šepić et al., 2015b), indicating that the simultaneity of events can appear even at very large scales.

In this paper, we perform global analyses of the NSLOTT signal using multiannual and decadal series from 331 tide gauges coming from the MISELA dataset (Zemunik et al., 2021b). With this approach, we also construct a global climatology of moderate and extreme NSLOTTs and estimate their seasonality, spectral characteristics and regional synchronicity. In Section 2, we describe the data and methods used in the analyses, while Section 3 presents the results on the selected global distribution of the NSLOTT variables. The results are intensively discussed in Section 4. The paper finishes with the main conclusions listed in Section 5.

2. Data and methods

2.1. The MISELA dataset

The high-frequency sea-level data used in the present analyses were obtained from the MISELA dataset (Zemunik et al., 2021b), which contains sea-level records from numerous tide gauges worldwide and is designed to study atmospherically driven phenomena at tsunami timescales. The MISELA dataset is currently the only dataset that encompasses global sea-level measurements of research quality sampled at a 1-min resolution. The dataset consists of quality checked high-frequency sea-level records from 331 stations, the majority of which are based on raw data provided by the Intergovernmental Oceanographic Commission (IOC) Sea Level Station Monitoring Facility (SLSMF) reachable from http://www.ioc-sealevelmonitoring.org. The quality control procedures used in the construction of the MISELA dataset included (i) the removal of the tidal signal with T_Tide software (Pawlowicz et al., 2002), (ii) automatic spike detection procedures that detect out-of-range values and values deviating from a fitted spline (Williams et al., 2019a), (iii) the visual inspection of the detided series to remove low-quality data, (iv) the exclusions of the records observed during seismic tsunamis, (v) the linear interpolation of data gaps shorter than one week, and (vi) the filtering of the quality checked series to restrict the high-frequency ($T < 2$ h) sea-level signal using the Kaiser-Bessel filter (Thomson and Emery, 2014). The dataset and the quality check procedures are described in detail by Zemunik et al. (2021b).

The set of stations used in the presented analyses (Fig. 1) covers the coasts of all continents, and thus, the MISELA dataset has a satisfactory spatial distribution for global research. In different areas of the world ocean, data series vary in length, spanning from 2004 to 2019. To perform a robust statistical analysis, the stations were grouped into 20 different regions (Fig. 1). Table 1 shows that regions of South America and Western North America have the highest number of stations (34 and 32, respectively) among all regions. Particular areas are larger than others, e.g., Western North America contains three times more stations and consequently a cumulative time series length that is three times higher than that of Northern Europe. Interestingly, particular regions contain long records, e.g., the Baltic and Australia with a mean time series length of approximately 12 and 10 years, and therefore have a high cumulative time series length, which is even higher than some regions with more stations (e.g., Eastern Mediterranean). Regions of Central America – Pacific Coast, Northwest Africa, South Africa and Indian Ocean – Northern Coast have the lowest number of stations and station-years due to the poorer station coverage, demonstrating the well-known issue of underdeveloped sea-level networks in these areas (Woodworth et al., 2007, 2016). It can also be noted that for vast coastal areas, e.g., the northern coasts of Canada, Scandinavian countries and Russia (in fact, the entire coast of Russia), the UK and Ireland, Antarctica, the Middle East, and a better part of the African coast, there are no data in the MISELA database. In some areas (the northern coasts

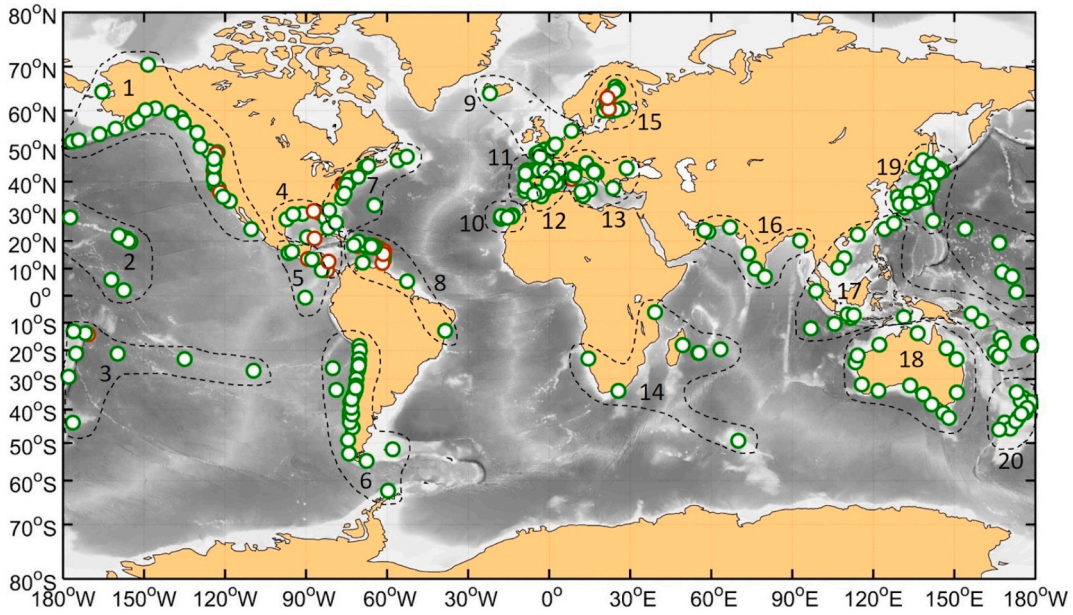

Fig. 1. Locations of the tide-gauge stations from the MISELA dataset used in the analyses. Green circles represent stations used in the spectral analysis, while red circles represent stations omitted from the spectral analysis. The borderlines between the analysed areas are denoted. (For interpretation of the references to colour in this figure legend, the reader is referred to the web version of this article.)

Table 1
Number of stations, cumulative length of time series (years) and mean length of time series (years) used in the analyses in each region.

	Number of stations	Cumulative length of time series (years)	Mean length of time series (years)
World	331	2303.04	6.96
1. Western North America	32	256.03	8.00
2. Hawaii and Central Pacific	14	114.90	8.21
3. South Pacific	10	72.20	7.22
4. Gulf of Mexico	11	77.05	7.00
5. Central America – Pacific Coast	6	21.81	3.64
6. South America	34	176.09	5.18
7. Eastern North America	18	126.22	7.01
8. Caribbean	29	173.33	5.98
9. Northern Europe	11	79.16	7.20
10. Northwest Africa	6	48.25	8.04
11. Western Europe	24	139.60	5.82
12. Western Mediterranean	19	150.57	7.92
13. Eastern Mediterranean	17	93.12	5.48
14. South Africa	8	51.89	6.49
15. Baltic	13	154.78	11.91
16. Indian Ocean – Northern Coast	7	31.32	4.47
17. South-East Asia	22	135.12	6.14
18. Australia	14	138.48	9.89
19. North-West Pacific Coast	22	156.89	7.13
20. New Zealand	14	106.25	7.59

of Europe, Asia and North America, as well as Antarctica and Africa), this is due to the following: a lack of stations in these vast, mostly uninhabited spaces; the inadequate station sampling resolution (in the UK and Ireland), and data-sharing policies, i.e., data nonavailability through the IOC SLSMF website (Russia).

To obtain zonal patterns of high-frequency oscillation characteristics, stations were grouped by 10° of latitude (Fig. 2); herein, the station-

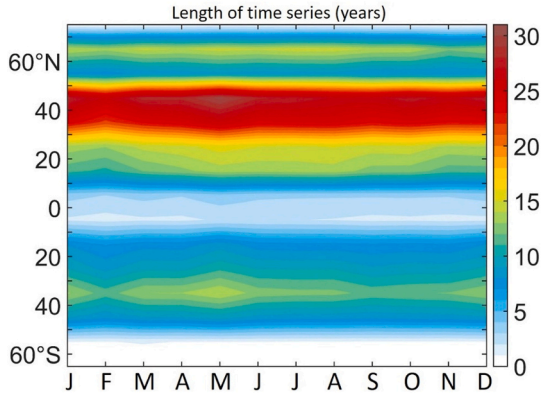

Fig. 2. Monthly distribution of a cumulative length of time series (in years).

richest zonal belts are in the mid-latitudes. In particular, this refers to 40–50° N, where 69 stations were operational, while the data-richest zonal belt in the Southern Hemisphere is 30–40° S, where 27 stations were operational. Tropical regions, as well as polar belts, are characterised by the largest data deficit. More precisely, the uppermost belts (70–80° N and 60–70° S) contain only one station per belt. The Northern Hemisphere dominates over the Southern Hemisphere in the total number of stations (233 out of 331 stations are located in the Northern Hemisphere) and, consequently, in the cumulative length of the time series. The number of stations over the months is nearly constant and is slightly higher during spring in the mid-latitudes (Fig. 2).

2.2. Methods

First, all data marked as interpolated in the MISELA dataset were excluded from the series, except for sequences with lengths of up to 5 min. The latter are considered too short to affect the results, and furthermore, if excluded, the series would become overly gap-dense, and the analyses that cannot treat data gaps (e.g., envelope of a series, spectral analysis) could not be properly performed. Furthermore, hour-long data adjacent to data gaps, as well as data sequences shorter than 6

h and surrounded by the data gaps, were also removed due to the unreliability of the filtering procedure, spectral analysis, and envelope estimation at data borders.

From each high-frequency sea-level series, three variables were computed: (i) the variance of the signal, (ii) the range of high-frequency sea-level oscillations (median and 99.99th percentile) and (iii) the *Z*-score of the range. The range of the high-frequency signal was estimated in each time step by calculating the Euclidean distance between the upper and lower envelopes of the series and determined by spline interpolation over selected local maxima and minima, respectively, by using the MATLAB function *envelope* (Fig. 3). The envelope is a smoothed curve or signal amplitude that encompasses selected local extrema from the input signal, which is initially developed (among others) for the analysis of seismic recordings (Farnbach, 1975). The parameter *sample numbers* of the peak-type envelope function, which determines how many time steps separate the selected local extrema, vary between 5 and 30 and are chosen for each station individually by visually checking the goodness of the envelope fit on the sea-level time series. At each station, the moderate (average) sea-level range is calculated as the median of all ranges, while the 99.99th percentile of the ranges represents the extreme range of high-frequency oscillations.

To compare the extreme with the moderate oscillations for non-Gaussian distributions, the Z-score was calculated as follows:

$$Z = \frac{p - med}{mad} \quad (1)$$

where p is the 99.99th percentile of the range, *med* is the median of the range and *mad* is the median absolute deviation of the range, which is defined as the median of the absolute deviations of the ranges from the median of the range. Such a score measures an outlier strength and is more robust than the score based on a mean and standard deviation of a data sample; the latter is plausible for Gaussian distributions only (Leys et al., 2013).

To quantify the frequency characteristics of the most extreme NSLOTTs, the ten strongest and ten weakest NSLOTT events were extracted at each station, which are further referred to as *extreme NSLOTT events* and *background NSLOTT events*, respectively. The station-based events are defined by the variance over 24-h-long data windows containing no more than 10% of the data gaps, where the ten highest and ten lowest values of variances were ascribed as extreme NSLOTT events and background NSLOTT events, respectively. Furthermore, the minimum temporal distance between events is chosen as 24 h. Fig. 3 visualises the NSLOTT record from 2014 at South Beach, Oregon, US, with one isolated extreme NSLOTT event and one background NSLOTT event.

To assess the sea-level spectrum of a selected event, Welch's method for the estimation of power spectral density was applied (Thomson and Emery, 2014) using a 17-h-long Kaiser-Bessel window with 50% overlap. Among 331 stations, 23 were excluded from the spectral analysis due to either a lack of daily data windows with less than 10% data gaps or different problems within the spectra (e.g., aliasing). At each station, the power spectral density was estimated for each extreme and background NSLOTT event. Then, the medians of the spectra of ten extreme and ten background NSLOTT events were estimated at each frequency. In addition, the ratio between the extreme NSLOTT event spectrum and the averaged background spectrum was calculated to assess the amplification of energy during extreme events. The median of these ratios was also estimated at each station. Several additional characteristics of the spectra were calculated: (i) an integral of the spectrum representing the total amount of energy over all frequencies and (ii) a slope of a line linearly fitted to the logarithmic spectral curve between 2 min and 2 h

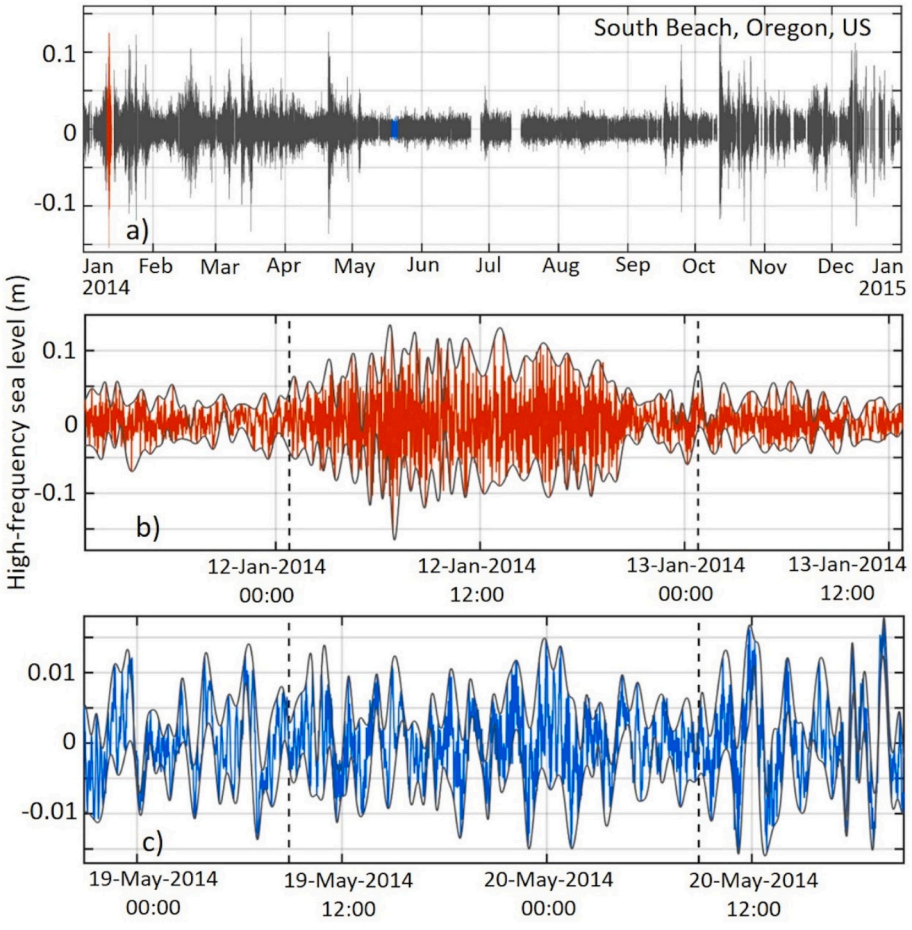

Fig. 3. High-frequency sea-level series from the station at South Beach, Oregon, US, during a) 2014, and magnified to b) an extreme (red) and a background (blue) NSLOTT event, together with lower and upper envelopes (grey) used for the estimation of the NSLOTT range. Black vertical dashed lines denote the 24-h extreme and background events that are used in the analyses. (For interpretation of the references to colour in this figure legend, the reader is referred to the web version of this article.)

periods to quantify the behaviour of energies at the examined frequencies. Peaks in a spectrum were extracted using the MATLAB function *findpeaks* in the following way: (i) the base for each local maximum was estimated by calculating the difference between the value of the peak and its prominence, which measures how much the peak stands out relative to its height and position towards the other peaks, and (ii) peaks at least ten times larger than the base were selected, hereafter referred to as peaks in the spectra. The spectra of the extreme NSLOTT events, as well as the ratios with the background event spectra, were then classified into 6 categories: decreasing, constant and increasing, each with at least one peak or without any peak. Here, the spectrum is considered constant if the slope is in the interval of −0.3 to 0.3, as this is a narrow interval that is approximately 0 and is chosen to represent quasi-constant spectra. The bordering values are based on the probability distribution of the spectral slopes, resulting in ~20% of constant slopes. Furthermore, the spectrum increases if the slope exceeds 0.3 and decreases if the slope is below −0.3. The same thresholds are chosen for the slope of the spectral ratio. It should be noted here that lines are linearly fitted to the logarithmic values of energy and energy ratios (Fig. 8); therefore, the unit of the slope of the spectra is log(cm^2/cph)/log/(cph), and the unit of the slope of the spectral ratio is 1/log(cph).

To investigate the synchronicity in the occurrence of extreme NSLOTT events in an area, their overlap at nearby stations was quantified. This analysis has been motivated by the documented properties of NSLOTTs – they often occur over larger or smaller regions during a certain period (up to a few days). Such behaviour resembles atmospheric

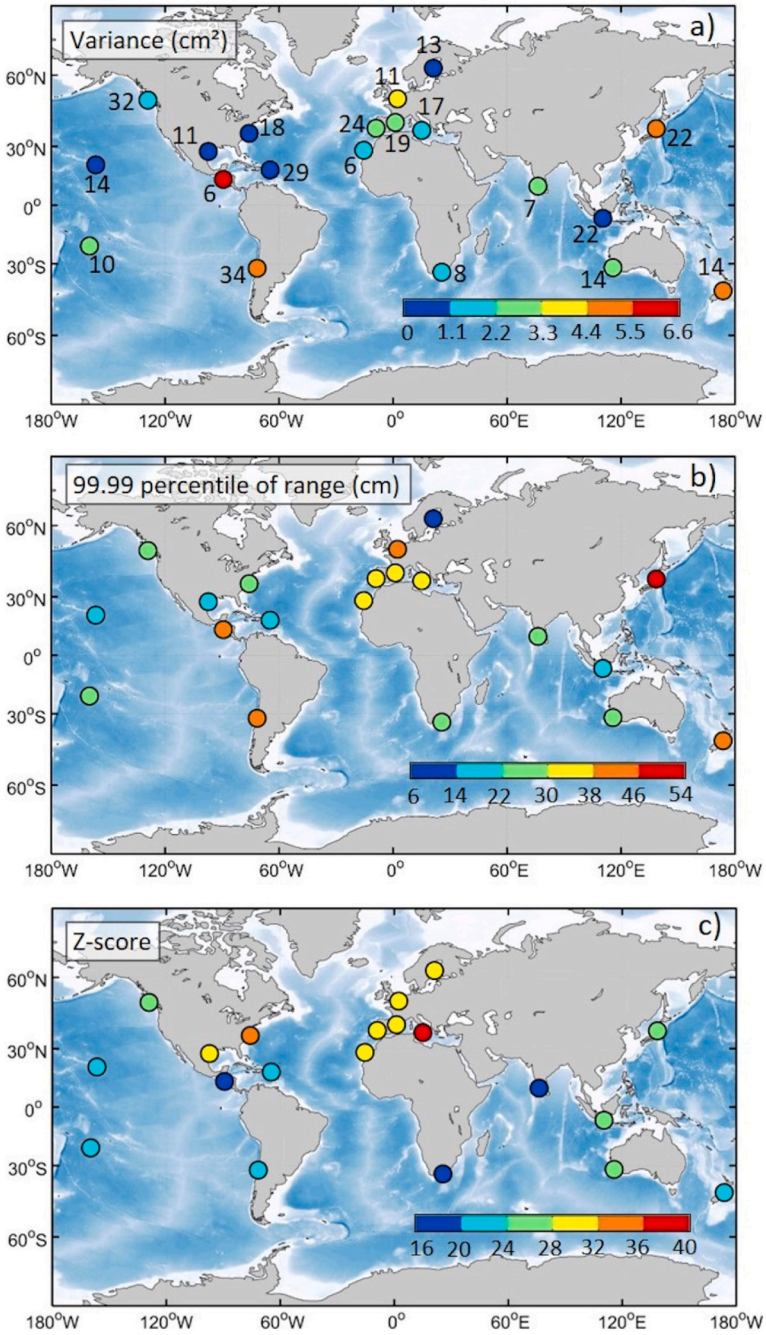

Fig. 4. High-frequency sea-level a) absolute variance, b) 99.99th percentile of the range and c) Z-score, all regionally averaged. The numbers near circles in the uppermost panel denote the numbers of tide-gauge stations in the respective areas.

forcing that is generating NSLOTTs and has been described in the Mediterranean (Šepić et al., 2009, 2015a), northwest Europe (Williams et al., 2021a), western Australian coastline (Pattiaratchi and Wijeratne, 2015), and the US east coast (Pasquet et al., 2013; Dusek et al., 2019), yet never at the global scale. To overcome this issue, the synchronicity index of the extreme NSLOTT events was defined for any Station *S* as the ratio of the following variables: (i) the number of cases in which the extreme NSLOTT event at Station *S* was conjoined with the extreme NSLOTT event at any other station in a circle of radius *R* and in a time interval [−48 h, 48 h] around the event, and (ii) the total number of possible conjunctions of extreme events at all stations in a circle of radius *R*. With such a definition, the synchronous occurrence of the extreme NSLOTT events may be quantified over variable geographical regions – here, the radii *R* are 250, 500 and 1000 km. The synchronicity index equals 0 if no extreme NSLOTT events were found at any neighbouring station in a circle of radius *R* and equals 1 if the extreme NSLOTT events were found at all neighbouring stations in a certain time interval: 96 h. Additionally, the time interval between the overlapping extreme NSLOTT events normalised by the distance between the stations is estimated and averaged for any Station *S*.

3. Results

3.1. Global variances and ranges

The spatial distribution of the NSLOTT absolute variance, the 99.99th percentile of the range and the *Z*-score of the range averaged over the prescribed regions are plotted in Fig. 4. The NSLOTT variance reaches 6.57 cm^2, which implies that the average energy of high-frequency sea-level oscillations is generally not as high as that of other sea-level components (e.g., a few orders of magnitude lower than tidal energy (Haigh et al., 2019) or storm surges (Muis et al., 2020)). The highest values are found in Central American regions, i.e., the Pacific Coast (6.57 cm^2) and Northwest Pacific Coast (4.79 cm^2), while the lowest values are obtained for the Gulf of Mexico (0.56 cm^2) and the Baltic regions (0.25 cm^2).

Despite the fact that their average energy is not large, the NSLOTTs can reach great heights (> 4 m) during most extreme episodes (i.e., meteotsunamis) (Rabinovich, 2020). The station-averaged NSLOTT range of extreme oscillations (99.99th percentile of the overall NSLOTT range) exceeds half a metre in the region of the Northwest Pacific Coast (Fig. 4b), followed by the regions of South America, the Pacific Coast of Central America, Northern Europe and New Zealand, with values greater than 40 cm. Moreover, the extreme oscillations can be as high as one metre at certain stations, such as Nagasaki, Japan, and Lampedusa, Italy, where the 99.99th percentiles of the NSLOTT range reach 105 and 97 cm, respectively (Table 2).

The *Z*-score, which quantifies the difference in the strengths of extreme and moderate NSLOTTs (i.e., the difference in the NSLOTT distributions), shows that the highest values are in the Mediterranean and other European regions and along the east coast of North America (Fig. 4c). Specifically, the *Z*-score in the Eastern Mediterranean reaches 40, meaning that the range of oscillations may be 40 median absolute deviations higher than the median range during extreme episodes, and even more at some stations, such as Split, Croatia and Lampedusa, Italy, where the *Z*-scores reach 79 and 62, respectively (Table 2). This implies that the extreme NSLOTT may be enlarged tens of times during extreme events and therefore threaten coastlines, particularly in low-tidal regions such as the Mediterranean, as stated by Vilibić and Šepić (2017).

The NSLOTT variance, the 99.99th percentile of the range and the Z-score all have a similar zonal pattern, with lower values in the tropical and polar regions and higher values in the mid-latitudes (Fig. 5). The only exception to this zonal pattern is that the Z-score reaches a maximum in the northernmost zonal belts (60–80°N). It should be highlighted here that marginal zonal belts, both southern and northern, contain only one station; therefore, the statistics are not as robust as those for the other belts. Zonally averaged values of the NSLOTT variance and the 99.99th percentile of the range are four to five times higher in the mid-latitudes than in the tropical areas, peaking in the Southern Hemisphere. In contrast, the zonal curve of the Z-score shows higher values in the northern mid-latitude belts than in the southern belts, suggesting that although higher oscillations are recorded at the tide gauges in the Southern Hemisphere, a higher amplification of extreme oscillations is observed in the Northern Hemisphere.

3.2. Seasonal patterns

Fig. 6 shows the month in which the highest range of a moderate (median) and extreme (99.99th percentile) NSLOTT is recorded. A clear seasonal maximum of the moderate oscillations is observed throughout the winter season in the mid-latitudes (December–February in the Northern Hemisphere and June–August in the Southern Hemisphere), encompassing 85% of all stations in these latitudes. A few anomalies are visible in the southern part of the Chilean coast, North Australia and in the Gulf of Mexico, while the tropical regions of the Indian and Mexican coasts show the highest values during the rainy seasons. The different distribution of months with the 99.99th percentile NSLOTT maximum in Fig. 6b shows that the extreme NSLOTT values do not follow such an exact seasonal pattern in most mid-latitudes. Precisely, the maximum of extreme NSLOTT values is quasi-equally occurring in different seasons (57% during winter and 43% during summer). Nevertheless, the west coast of North America maintains clear winter maxima of the extreme NSLOTT values, while in Northern Europe, the Northwest Pacific Coast and South American extremes also prevail in winter but are interrupted

Table 2
Stations with the highest 99.99th percentile values of the NSLOTT range, the highest median values of the NSLOTT range and the highest Z-score values.

Station name	99.99the percentile of NSLOTT range [cm]	Station name	Median of NSLOTT range [cm]	Station name	Z-score
Nagasaki, Japan	104.6	Bucalemu, Chile	15.7	Lawma, Amerada Pass, Louisiana, US	87.9
Lampedusa, Italy	97.4	Bahia Mansa, Chile	11.8	Castro, Chile	84.9
Minami-Tori-Shima, Japan	89.8	La Libertad, El Salvador	10.6	Split, Croatia	79.4
Juan Fernandez, Chile	82.7	Cape Cuvier Wharf, Australia	10.0	Magueyes, Island, Puerto Rico	77.5
San Felix, Chile	82.1	Port Elizabeth, South-Africa	9.7	Hienghene, New Caledonia	68.0
Port Napier, New Zealand	78.7	San Felix, Chile	9.1	Apalachicola, Florida, US	66.5
Bucalemu, Chile	77.8	Calais, France	9.0	Prince Rupert, Canada	65.0
Rudnaya Pristan, Russia	75.7	Jackson Bay, New Zealand	8.5	Tarifa, Spain	63.9
Atlantic City, New Jersey, US	75.0	Puerto Angel, Mexico	8.5	Cordova, Alaska, US	62.7
Iquique, Chile	74.8	Salina Cruz, Oaxaca, Mexico	8.4	Lampedusa, Italy	61.6

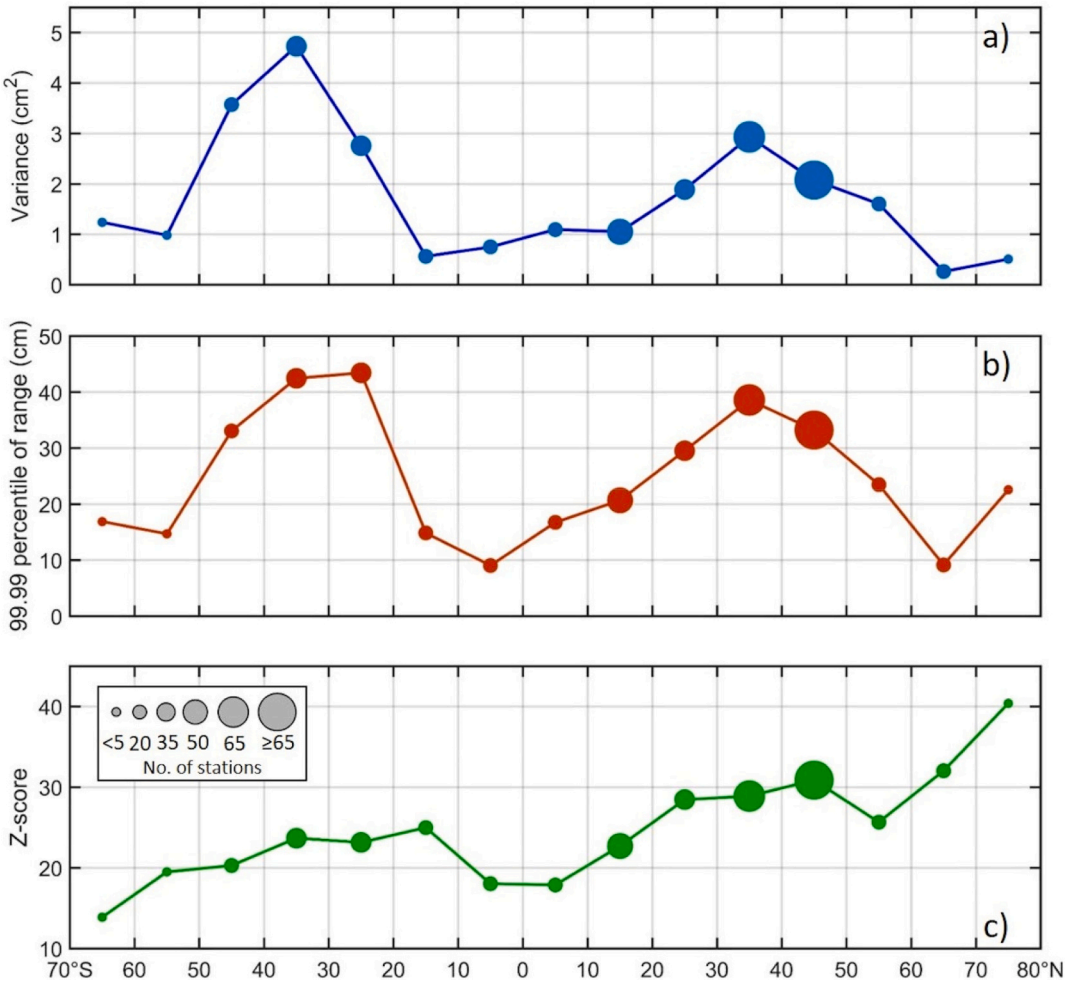

Fig. 5. High-frequency sea-level a) absolute variance, b) 99.99th percentile of the range and c) Z-score, all averaged over 10° zonal belts. The size of each circle is proportional to the number of tide-gauge stations in the respective zonal belt.

by the spring and summer months at some stations.

Fig. 7 further quantifies a strong domination of the winter NSLOTT in the mid-latitudes–both moderate (median) and extreme (99.99th percentile). In the case of the extreme NSLOTT (Fig. 7b), nearly half a metre range is observed in the 30–40°S zone in July. The moderate NSLOTTs (Fig. 7a) peak in the same zonal belt. However, they show a less developed seasonal cycle and a milder transition between seasons, retaining high values during all seasons. Another peak is evident in winter and early spring in the 20–40°N zone, with heights of moderate oscillations up to 3.5 cm and heights of extreme oscillations up to 35 cm.

3.3. *Spectral characteristics of extreme NSLOTT events*

Fig. 8 displays spectra computed for selected extreme and background NSLOTT events from the sea-level records measured at the stations in South Beach (USA), Mejillones (Chile), Almeria (Spain), Tosashimizu (Japan) and Burnie Tasmania (Australia). The stations were selected as representative stations of the coherent regions with good longevity (i.e., time series spanning a decade) of high-quality sea-level series. It should be highlighted that the spectra and spectral ratios represented by thick blue, black and red lines in Fig. 8 come from statistics (median) of the spectra based on ten single extreme and background NSLOTT events and their ratios. Therefore, these lines are smoother than spectra of individual events and do not contain instrumental noise, unlike single-episode spectra represented by thin grey lines. Several interesting properties can be noticed for these stations: (i) the averaged spectra of the strongest selected episodes contain the main energy at lower frequencies (corresponding to periods higher than 15 min) and decrease with increasing frequency, (ii) the majority of spectral peaks are observed at very high frequencies (corresponding to periods up to 6 min), and (iii) the background spectra (spectra averaged over the weakest episodes) have approximately the same energy distribution as the spectra of the strong episodes but with milder peaks and up to 4 orders of magnitude lower energy. The ratios between the spectra of the extreme NSLOTT events and the background spectra show a more monotonic energy distribution and even an increase in the energy ratio at higher frequencies, such as at the station in South Beach, Oregon, US.

Global spectra of extreme NSLOTT events averaged over all 308 stations used in the spectral analysis (Fig. 9) confirm the decrease in the energy with increasing frequency over the whole distribution of spectra (1st, 10th, 50th, 90th and 99th percentiles of energy). The energy decrease with frequency is the steepest at stations with a low energy content and mildest at stations with a high energy content. The energy of the extreme NSLOTT events can vary up to 5 orders of magnitude at different stations for a particular frequency. In contrast, the ratio between the extreme NSLOTT event spectra and the background spectra increases with the frequency, particularly for the stations with a high energy difference between the extreme and background NSLOTTs (i.e., for the 99th percentiles of spectral ratios). The exceptions are stations with lower ratios (to the 10th percentile). Therefore, the amplification of the NSLOTT is much more pronounced in periods smaller than 10 min (corresponding to 6 cph) than it is in longer periods.

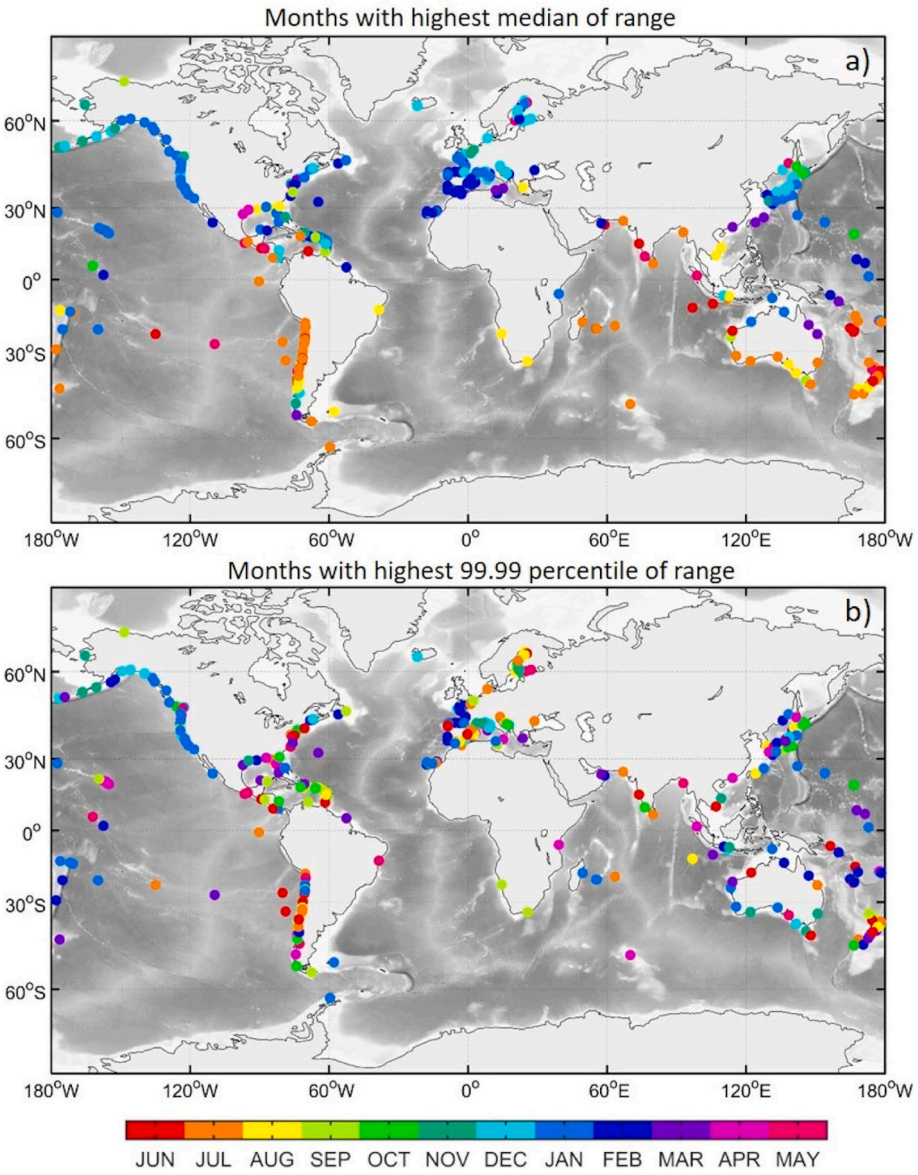

Fig. 6. Global map of months with maximal a) median and b) 99.99th percentile values of the high-frequency sea-level range.

In Fig. 10, the decreasing and constant spectra with at least one spectral peak dominate over the entire world ocean. Only 5% of the stations have increasing spectra (with a slope higher than 0.3) over the NSLOTT frequency band, and these are scattered across the regions. Spectra without any peaks are very rare and are visible at several stations in the Pacific Ocean, at stations along the east coast of the US and in a few other locations and are mostly located along the open coastline. Energy generally increases in periods ranging from 15 to 60 min, peaking at 30 to 40 min. There is no spectral ratio without a peak, implying that each station has an amplification of energy during extreme episodes at some period (Fig. 11a). Interestingly, there is approximately the same number of stations with positive and negative slopes of the spectral ratio, meaning that at some locations, a larger amplification of the energy occurs at lower frequencies (the Australian and Japanese coasts and the Mediterranean and Baltic Seas), while at others, it occurs at higher frequencies (the west coast of the US, New Zealand, and western and northern Europe).

The total amount of energy of the extreme NSLOTT events shows a similar zonal pattern to the total NSLOTT variance and the NSLOTT range, peaking in the mid-latitudes and decreasing in the tropical and high-latitude belts (Fig. 12a). The resemblance is also evident for the ratio of the energy during the extreme and background events, which points to the higher NSLOTT amplification rates in the mid-latitudes, as inferred by the *Z*-score analysis.

3.4. Synchronicity of extreme NSLOTT events

For each station, the synchronicity index was calculated and further zonally averaged. Furthermore, the average time interval between the synchronized extreme NSLOTT events at the corresponding station and a nearby station relative to their distance was calculated and zonally averaged. Fig. 13 illustrates the zonal distribution of the index and the time interval for the radii of 250, 500 and 1000 km, in which the synchronization of events is observed. It is evident that the highest synchronicity index is observed for the radius of 250 km, meaning that although the smallest radius contains the lowest number of stations in the vicinity of the considered station, extreme episodes tend to overlap more frequently than in the case of a larger radius. Specifically, the extreme NSLOTT events occurring in the mid-latitudes are synchronous at nearby stations in 20% to 32% of all extreme NSLOTT events on

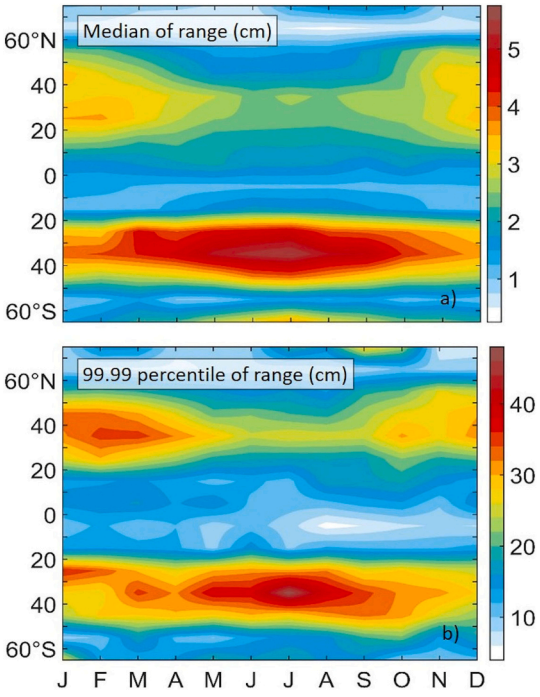

Fig. 7. Monthly distribution of a) the median of the range and b) the 99.99th percentile of the range of the high-frequency sea-level oscillations, which are all averaged over 10° zonal belts.

average. The averaged synchronicity index is somewhat lower in the mid-latitudes for the synchronicity radii of 500 and 1000 km, where 15–24% and 6–20% of extreme NSLOTT events are synchronous, respectively.

Analogously, the average normalised temporal distance between the episodes identified as synchronous, relative to the distance of the coherent stations, reaches the highest values for the smallest radius. For the radius of synchronicity of 250 km, the value of 0.04 h/km in the mid-latitudes of the Northern Hemisphere (20–40° N) indicates that approximately 6 h is needed on average for the extreme NSLOTT events to occur at the two stations that are 150 km apart; this quantifies the average speed of the pattern that generates the extreme NSLOTT as approximately 7 m/s. This value is several times lower than the propagation speed of synoptic systems and frontal zones in the mid-latitudes (Ulbrich et al., 2009), suggesting that the systems that generate extreme NSLOTTs are slower than an average extratropical cyclone. The same behaviour occurs when increasing the synchronicity radii to 500 and 1000 km. In the tropical and high-latitude zones, either no stations are found within the appropriate distance radius, or the synchronicity index is zero (no overlapping of events is recorded); therefore, the values of the normalised time interval that are needed to propagate NSLOTT events between stations are absent in those zones.

4. Discussion

4.1. Global variances and ranges

The analysis of the variance, the 99.99th percentile of the range and the Z score of the range of the high-frequency sea-level oscillations allow us to discuss several items. Generally, the estimated NSLOTT variance is clearly not high, having station-averaged values up to 6.6 cm^2. Vilibić and Šepić (2017) claim that the contribution of the NSLOTT variance to the overall variance reaches only 1.25%. The contribution is asserted to be somewhat larger in the low tidal basins, for instance, in the Mediterranean Sea, where Šepić et al. (2015a) found that it reaches 9.5%. However, vigorous high-frequency sea-level oscillations may appear during extreme events (i.e., meteotsunamis) with ranges exceeding half a metre in some regions and a few metres at certain stations, even surpassing the tidal signal (Rabinovich, 2020). Previous findings showed that the NSLOTT variance percentage in a total signal can increase up to 50% when analysing strong episodes at meteotsunami hotspots, revealing the importance of the high-frequency signal when assessing global sea-level extremes (Vilibić and Šepić, 2017).

In this study, as the MISELA dataset contains only the high-frequency part of the sea-level signal (Zemunik et al., 2021b), the NSLOTT variances and ranges are not assessed in comparison with the overall variances. Therefore, a comparison has been made of the tidal ranges coming from the EOT20 global ocean tide model (Hurt-Davis et al., 2021). Precisely, the maximum range of astronomical tides has been used for estimating the tidal range, defined as the sum of the doubled amplitude of tidal constituents provided for the model grid point nearest to a tide gauge station. Fig. 14, which contains the ratio between the NSLOTT 99.99th percentile and the tidal range at each station, shows that the values of the ratio are mainly consistent among the stations located along the same coasts and follow the global distribution of the tidal range (Hill, 2016). For example, the west coast of North America and Northern Europe have some of the highest tides in the world, and therefore, the proportion of the NSLOTT range to the tidal range is low – mostly up to 0.05 and sometimes up to 0.1. Ratios are evidently the highest in microtidal regions, such as the Mediterranean Sea and the Sea of Japan (Odamaki, 1989; Tsimplis et al., 1995). Additionally, these regions are recognised as meteotsunami hotspots where a significant portion of the world meteotsunami research has been carried out (e.g., Hibiya and Kajiura, 1982; Vilibić et al., 2021a; Jansà and Ramis, 2021). All the stations in the Mediterranean Sea have ratios higher than 0.2, with the exception of the northern Adriatic, where a higher tidal range results in a lower ratio, and a few stations in the Ligurian Sea. Furthermore, the two highest ratios are found at the Pantelleria and Lampedusa stations (1.01 and 10.4), which are very close to an amphidromic point (Abdennadher and Boukthir, 2006) and located on a shelf where intense high-frequency sea-level oscillations are known to occur (Candela et al., 1999).

The NSLOTT variances are found to differ even between the neighbouring stations, which is due to the bathymetry surrounding the tide gauges (Monserrat et al., 1998; Woodworth, 2017). Specifically, if the tide gauge is situated in a harbour or a bay, particularly in a cone-shaped bay with a narrow entrance, the oscillations might have a high capability for amplification due to internal resonance effects (so-called harbour resonance, Miles and Munk, 1961; Raichlen, 1966; Rabinovich, 2009; Denamiel et al., 2018). In contrast, the NSLOTT measured at a tide gauge located on the open coasts is influenced only by external processes, such as the Proudman resonance (Proudman, 1929) over wide shelves or shelf resonance over narrow shelves (Woodworth, 2017), and is dependent on the size of the shelf and complexity of the shelf break.

The range of the NSLOTT excited during extreme episodes is enlarged many times with respect to the calm periods. Nevertheless, the increase varies from region to region and presumably depends on the size of the shelf stretching in front of the affected area. The larger the shelf is, the larger the space on which the Proudman resonance takes place and consequently amplifies waves (Williams et al., 2021b). Thus, the *Z*-score values are evidently higher in regions with hundreds of kilometres of shelf offshore (e.g., Northern Europe and the US east coast). In contrast, the coast of Chile has a lower Z-score, and in conjunction with a higher absolute variance, suggests a larger persistence of the moderate NSLOTT in this area. The persistence of the NSLOTT there and at other open ocean coasts may also be due to wind-driven and infragravity waves, which normally act at open coasts in a more coherent way (Rawat et al., 2014; Melet et al., 2020).

Furthermore, a high Z-score and a low variance in the Mediterranean Sea indicate that high-frequency sea-level oscillations are characterised with occasional prominent episodes here rather than with permanency. This may be a consequence of specific synoptic conditions that drive the

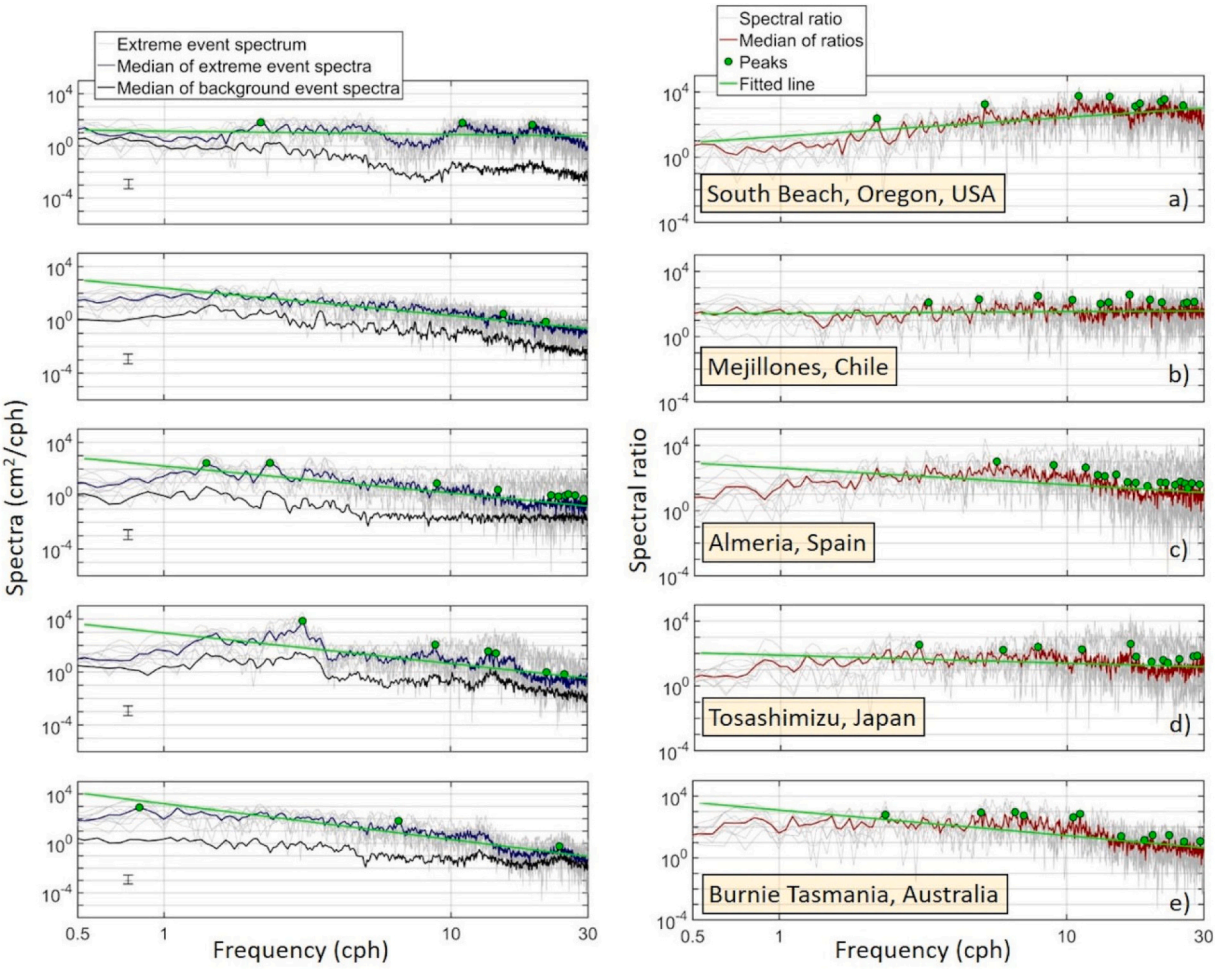

Fig. 8. Sea-level spectra computed for 10 extreme NSLOTT events (grey), their medians (dark blue), the medians of 10 background event spectra (black) (left), and ratio between the extreme NSLOTT event and background spectra estimated separately for each event (grey) and their medians (red) (right) for the following stations: a) South Beach, Oregon, US, b) Mejillones, Chile, c) Almeria, Spain, d) Tosashimizu, Japan, and e) Burnie Tasmania, Australia. The lines fitted to the spectra, spectral ratios and peaks have also been plotted (yellow). The 95% confidence interval of the spectra is marked in the left panels. (For interpretation of the references to colour in this figure legend, the reader is referred to the web version of this article.)

Mediterranean high-frequency oscillations. Precisely, Mediterranean meteotsunamis are mostly generated by the wave-duct mechanism (Monserrat and Thorpe, 1996), which requires the stability of the lower troposphere. This pattern resembles the observed synoptic patterns during the Mediterranean NSLOTT (Šepić et al., 2015a) and meteotsunamis (Jansà and Ramis, 2021; Vilibić et al., 2021a), in which dry and warm Saharan air penetrates towards the Mediterranean below a mid-troposphere jet located within a dynamically unstable atmospheric layer.

The variance and range are the highest in the mid-latitudes and lowest in tropical and polar regions, as already shown by Vilibić and Šepić (2017), who also found a significant correlation between the variance and maximal range of the NSLOTT, with the wind speed at the 500-hPa height. This might point to a global conjunction of the mid-tropospheric winds with the generation of the NSLOTT events. However, the atmospheric setup is beyond the scope of this paper, and the global quantification of the NSLOTT sources is still a question to be answered.

4.2. Seasonal patterns

The wintertime maximum of the median of the NSLOTT ranges in both the Northern and Southern Hemisphere mid-latitudes indicates their potential relation to the effects of the extratropical cyclones. Namely, the NSLOTT has been correlated with strong mid-tropospheric winds (Vilibić and Šepić, 2017), which are dominant features of the mid-latitude belts during the winter months (e.g., Hartmann, 2007). Furthermore, such statistics are in line with previous regional or local analyses, which place the maximum of high-frequency sea-level oscillations exactly during the wintertime, such as the analyses of NSLOTT and seiches carried out throughout the North Sea or in the Port of Rotterdam (de Jong and Battjes, 2004; Ozsoy et al., 2016).

The statistics become more complicated when assessing the extreme NSLOTT (99.99th percentile) seasonal distribution, which resembles documented regional or local seasonal distributions of meteotsunamis. Our results show that although the majority of moderate oscillations have the highest ranges during the winter season, this is not the case for the extreme NSLOTT, for which the highest ranges are recorded equally during the summer and winter months. Furthermore, there is a strong spatial incoherence in the domination of summer or winter extreme NSLOTTs (Fig. 6), which presumably reflects the influence of local effects (such as the orientation of the coastline and storm propagation directions) in shaping the extreme NSLOTT.

Most meteotsunami climatologies and research studies have focused on meteotsunami events that occurred in the summer season, as in the Mediterranean (Šepić et al., 2015a; Jansà and Ramis, 2021), the Finnish coast (Pellikka et al., 2020), the Great Lakes (Bechle et al., 2016) and the Australian shelf (Pattiaratchi and Wijeratne, 2014). However, the

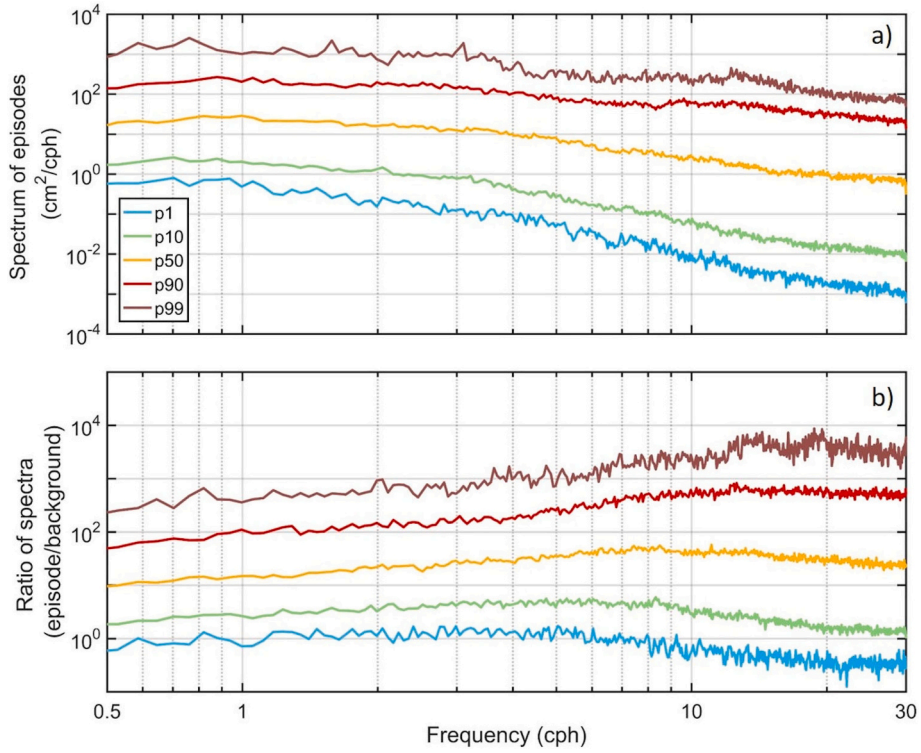

Fig. 9. 1st, 10th, 50th, 90th and 99th percentiles computed over all stations for a) the median of sea-level spectra of the selected extreme NSLOTT and b) the median of ratios between the spectra of the selected events and the background spectra.

extreme NSLOTTs along the western European shores have maxima in winter, which follows several regional climatology studies for meteotsunamis (Ozsoy et al., 2016; Williams et al., 2021a). Along some coastlines, peaks in the number of meteotsunami events may occur even in two seasons, such as along the US east coast, where meteotsunamis peak in both summer and winter (Dusek et al., 2019).

As research on meteotsunamis and extreme NSLOTTs is still largely performed on case studies rather than on continuous high-frequency data, the summer meteotsunamis may attract more attention, as they appear unexpectedly during months with stable weather conditions and may endanger beachgoers and boatmen. However, as reported by Williams et al. (2021a), case studies might not be fully representative of meteotsunami seasonality. Furthermore, the climatologies and seasonality of the most destructive meteotsunamis, in which substantial damage and human casualties may occur, are far from proper quantified at most locations, as the time intervals over which the high-frequency sea-level data are available are shorter than the recurrence of such events.

4.3. Spectral characteristics

Several items can be concluded from the global NSLOTT spectra estimates. As expected, the NSLOTT spectra at most locations decrease with increasing frequency, but with a lower log slope than documented for higher periods, i.e., for periods longer than 2 h. In these longer periods (from hours to days), the residual spectra largely follow the red noise slope, which is approximately −2 (e.g., Medvedev et al., 2020). However, the slope over the NSLOTT frequencies is much more variable, spanning between −3 and 0.5. This is the consequence of a variety of coastal topographic and bathymetric features, which may amplify the red noise signal in larger periods (e.g., larger harbours and bays, Woodworth, 2017, or wide shelves, Williams et al., 2021b), while sometimes small harbours and inlets may increase the energy in periods from minutes to tens of minutes (Thotagamuwage and Pattiaratchi, 2014). Furthermore, a large energy in periods of a few minutes may be the result of large vessels manoeuvring inside harbours (Shao et al., 2020) or large wave action and infragravity waves, particularly along coasts that are open to oceans (Merrifield et al., 2014; Neale et al., 2015).

Interestingly, a larger amplification capacity within periods of several minutes is normally associated with rather constant or weakly decreasing NSLOTT spectra. Furthermore, an absence of energy at higher NSLOTT frequencies is normally associated with low amplification potential, i.e., with a low ratio between NSLOTT extreme and background spectra.

Most of the analysed spectra are characterised by one or more spectral peaks (more than 90%), probably because the large percentages of tide gauges are situated inside a well-shaped harbour or bay, as they are more protected there. However, the most destructive meteotsunami events are normally restricted to harbours or regions with high amplification factors (Monserrat et al., 2006; Rabinovich, 2009), particularly to the tops of harbours. The quality factor, which is a measure of energy damping in the system (Miles and Munk, 1961), normally surpasses 10 in bays where the most destructive meteotsunamis occur, such as Vela Luka Bay (Denamiel et al., 2018). This is also true for other resonant processes acting over longer periods, such as tidal resonance, which might increase the tidal response by an order of magnitude in some basins (Arbic et al., 2007; Medvedev et al., 2020). Nevertheless, the energy might span a wide range of frequencies in cases of complex topographies, when there is an interplay between local harbour or bay amplification potential and an effect of resonance on the shelf off of the local hotspot (Zemunik et al., 2021c). Indeed, the overall energies over the NSLOTT frequencies may differ between tide gauge locations by 3–4 orders of magnitude, which are related to the overall capacity of the local and wider bathymetry to either amplify incoming ocean waves or allow for a more efficient transfer of energy from the atmosphere.

4.4. Synchronicity

Historically, meteorological tsunamis have been considered to occur at destructive levels, typically as isolated events and at a single location

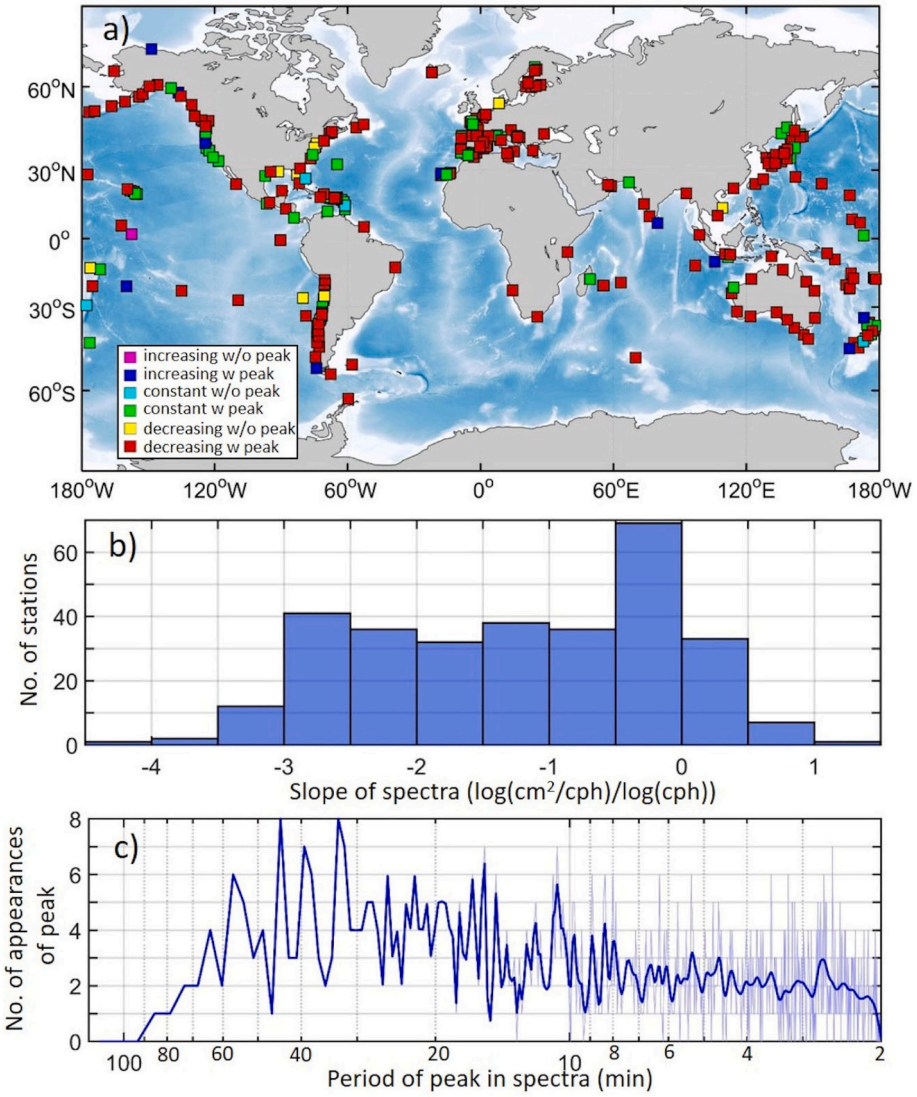

Fig. 10. Medians of the sea-level spectra of the selected extreme NSLOTT events: a) global map of the categories (increasing, constant, and decreasing, with or without peaks), b) distribution of the spectral log-log slopes, and c) number of appearances of peaks over periods (in minutes). Light blue denotes the original line, while dark blue denotes a smoothed line. (For interpretation of the references to colour in this figure legend, the reader is referred to the web version of this article.)

(Ewing et al., 1954; Orlić, 1980; Hibiya and Kajiura, 1982; Churchill et al., 1995). However, recent regional studies based on much better coverage of high-resolution data document that they might also appear quasi-simultaneously as a chain of events in a few adjacent locations across an entire coastline or even over a thousand kilometres (Šepić and Rabinovich, 2014; Šepić et al., 2015a). For selected events, Vilibić et al. (2021b) classify that approximately 35% of meteotsunamis have a spatial coverage over coastlines longer than 200 km. Based on high-resolution sea-level data, Šepić et al. (2015a) documented that extreme NSLOTT events occurred over most of the Mediterranean (from the Balearic Islands to Greece) during ~30% of events between 2008 and 2014, normally appeared sequentially at locations from west to east, and followed the eastward translation of meteotsunamigenic synoptic patterns. Šepić et al. (2009) found that NSLOTTs in the southern Adriatic Sea were conjoined with Balearic meteotsunamis in 50% of cases observed or recorded from 1975 to 1998, again due to the eastward propagation of synoptic formations that favour the generation of atmospheric gravity waves, clearly indicating regional synchronicity in meteotsunami events that has thus far not been documented on the global level.

Our results quantify the synchronicity of strong events while relying on the index linking extreme NSLOTT at nearby stations. The connection is the strongest in both the northern mid-latitude (30–60°N) and southern sub-tropical and mid-latitude (20–40°S) belts. The difference between the Northern and Southern Hemispheres is probably due to the different coastal morphologies and coastlines at which NSLOTT is recorded. The synchronicity index (for a 250 km radius) in the mid-latitude belts has median values between 20% and 32%, which is similar to the quoted Mediterranean studies. The northern mid-latitude synchronicity is more widely documented, both through statistics (quoted above) and through case study analyses. For example, a meteotsunami was observed along the Portuguese coastline in June 2010, propagating from south to north (Kim and Omira, 2021) over hundreds of kilometres. More recently, in 2017, the meteotsunami struck tourist beaches along the 500 km stretch of the coasts of the English Channel and North Sea (Sibley et al., 2021). Furthermore, the propagation of meteotsunami waves has been documented along Australia (Pattiaratchi and Wijeratne, 2014), the US east coast (Pasquet et al., 2013), western Europe (Williams et al., 2019b), and others.

Another application of the analysis of synchronicity may be for early warning systems during meteotsunami events. For example, Marcos et al. (2009) documented the occurrences of pronounced NSLOTTs at a

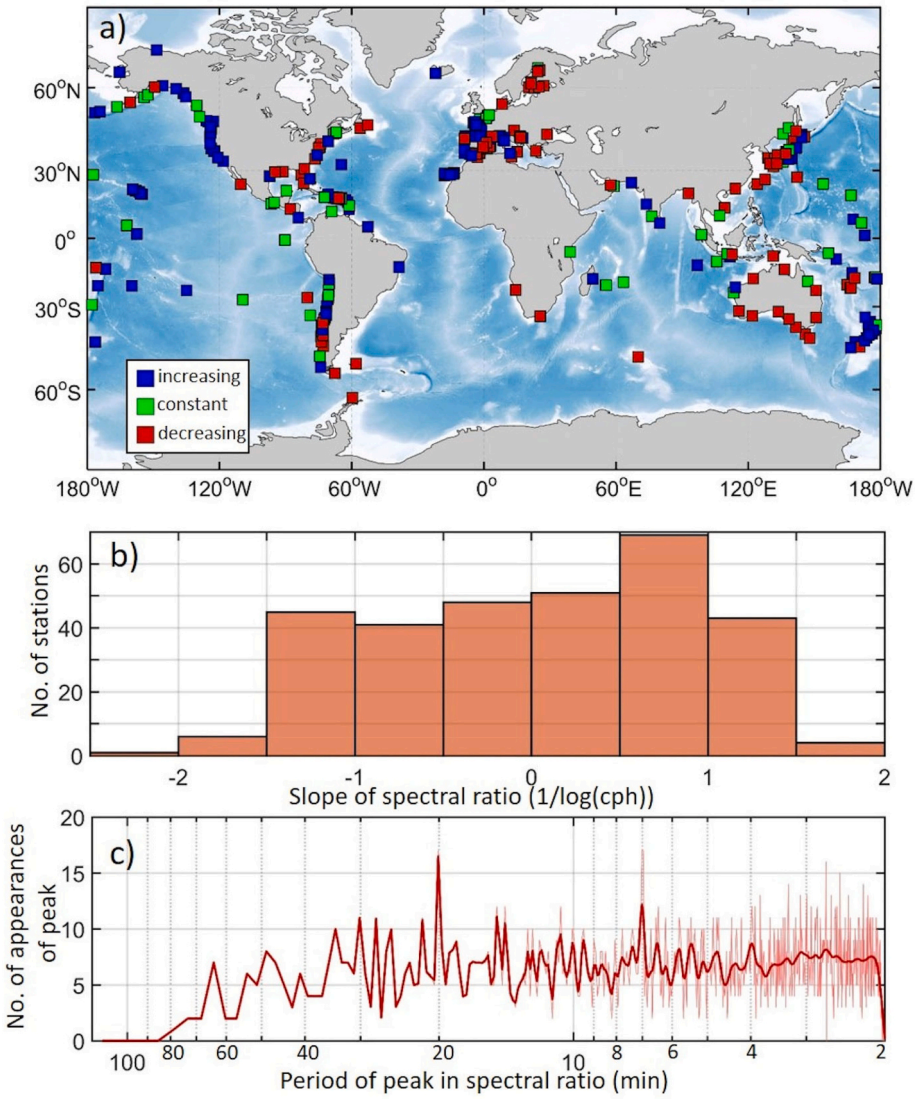

Fig. 11. As in Fig. 10, but for the median ratios between the sea-level spectra of the selected NSLOTT events and the background spectra.

station located approximately 40 min offshore of Ciutadella (the Balearic Islands), which is a known meteotsunami hot spot. The authors thus proposed using real-time assessments of NSLOTTs at this beacon station to provide meteotsunami early warnings for ports and inlets where such oscillations (and the associated currents) may affect navigation safety, coastal infrastructure and human lives. Consequently, stations with a high synchronicity index may be used for qualitative or quantitative forecasting of extreme meteotsunami events. Furthermore, as shown in the present study, more than one station may be considered for obtaining such relations with methods varying from simple multi-regression relations to more complex pattern recognition algorithms based on machine learning (Sun and Scanton, 2019).

4.5. Genesis and underlying processes

To understand the genesis of the NSLOTT at the global scale, two main questions should be answered: (i) What are the processes in the atmosphere that are responsible for the generation of the NSLOTTs in the ocean? and (ii) How does the NSLOTT propagate and amplify to generate meteotsunamis (i.e., the most extreme NSLOTT events) in coastal regions?

First, it may be reasonably assumed that these processes follow what is known of destructive meteotsunami events, which only occur at a limited number of coastal locations (Monserrat et al., 2006; Pattiaratchi and Wijeratne, 2015). It is known that meteotsunamis are generated when intense travelling atmospheric disturbances enter in resonance with long-ocean waves through the Proudman resonance (Proudman, 1929), the Greenspan resonance (Greenspan, 1956) or other mechanisms that are not yet fully documented. Finally, the waves generated offshore are amplified through topographic effects and coastal resonances, such as harbour resonance (Miles and Munk, 1961), which might substantially differ between harbours and bays and present important spatial variability on the order of a few kilometres (Monserrat et al., 1998; Rabinovich, 2009; Woodworth, 2017; Denamiel et al., 2018). Consequently, on the one hand, wider shelves may favour the generation of a pronounced NSLOTT due to their higher capacity for atmosphere-ocean resonances (such as the eastern coasts of the Americas, except the Caribbean, or the northwestern European shelf). However, complex coastal topographies are often conjoined with narrower shelves (such as the western coasts of the Americas), where channelling of long-ocean waves and harbour resonance may compensate for the lack of offshore atmosphere-ocean resonance. However, further research on the global maps of NSLOTT (and meteotsunami) bathymetry-driven generation potential must be undertaken to further document the various genesis processes involved.

The intensity and the energy content of the extreme NSLOTTs also

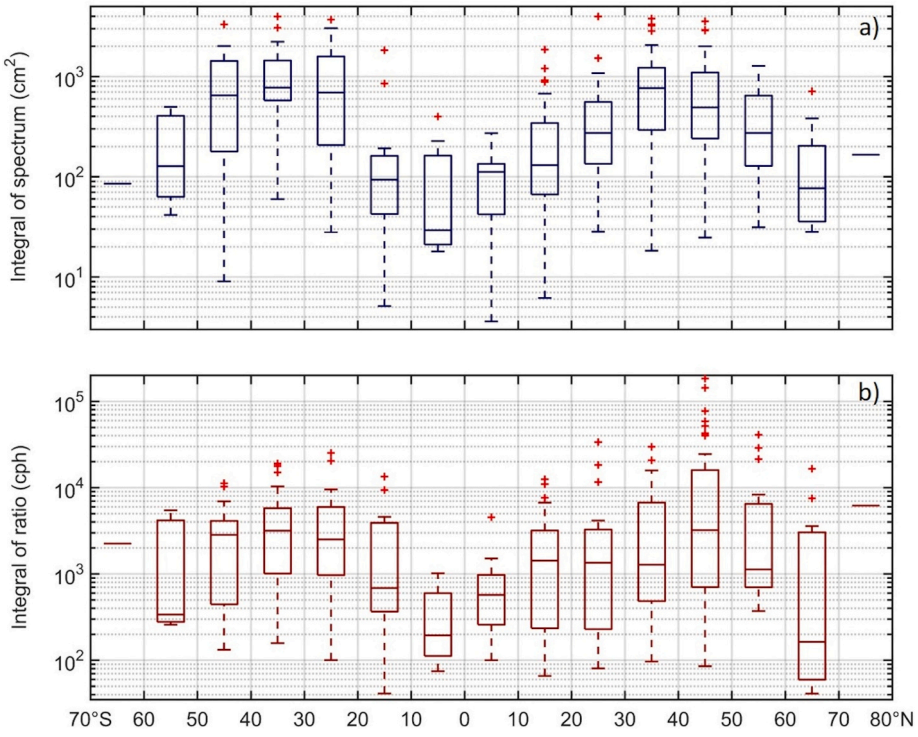

Fig. 12. Box-and-whisker plot of the a) median zonal energy of the selected extreme NSLOTT events and b) median energy ratio between the spectra of the selected events and the background spectra (computed as integrals of the spectra and the spectral ratios).

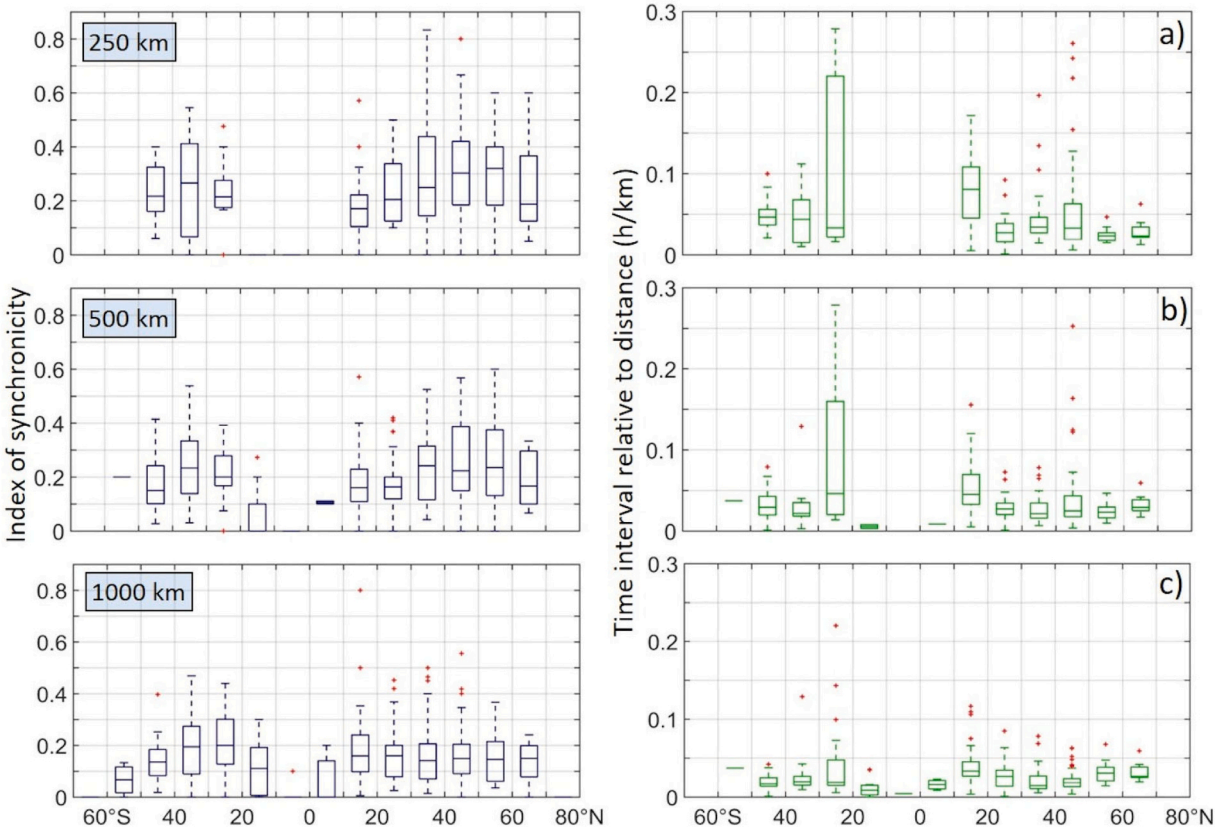

Fig. 13. Box-and-whisker plot of the index of synchronicity (left) and time interval (right) for the synchronization radii of a) 250 km, b) 500 km, and c) 1000 km.

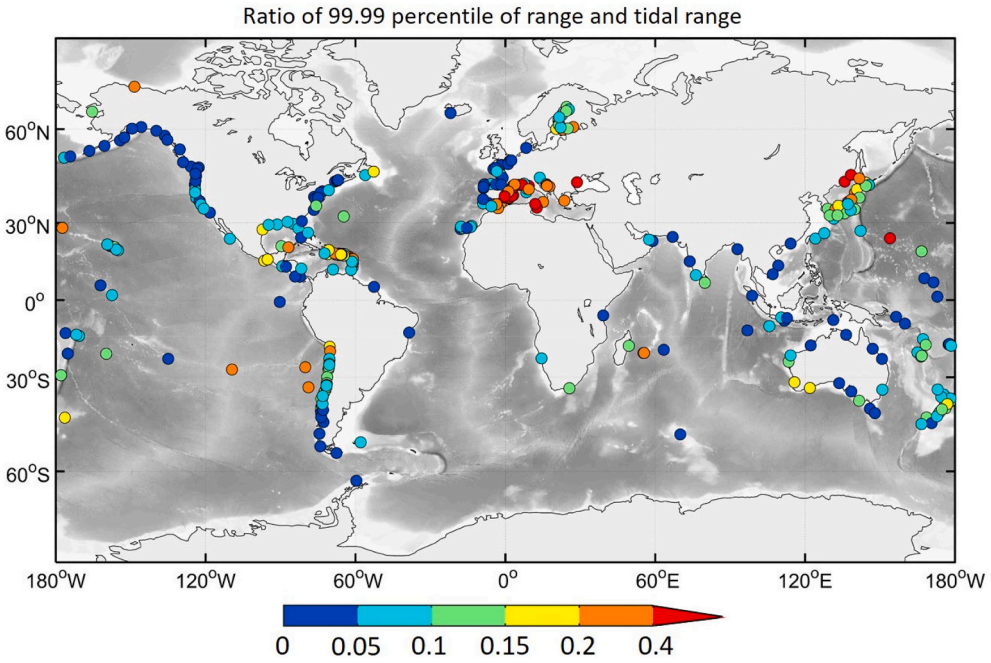

Fig. 14. Ratio between the 99.99th percentile of the NSLOTT range and the tidal range at each station. The tidal range is estimated from the EOT20 ocean tide model (Hurt-Davis et al., 2021).

depend on the characteristics of the travelling atmospheric air pressure and wind disturbances driving the atmosphere-ocean resonances: amplitude, propagation direction and speed, rate of change in space and time, longevity, dispersiveness, and spatial coverage. For meteotsunamis, these atmospheric disturbances are known to be associated with a number of atmospheric processes, such as squall lines (Churchill et al., 1995; Kazeminezhad et al., 2021), intense summer weather systems over the US called 'derechos' (Johns and Hirt, 1987; Šepić and Rabinovich, 2014), cold fronts (de Jong et al., 2003; Williams et al., 2021a), hurricanes and typhoons (Shi et al., 2020; Heidarzadeh and Rabinovich, 2021). In addition, identical to atmospheric internal gravity waves, wave ducting (Monserrat and Thorpe, 1996; Šepić et al., 2015b) and wave-CISK (e.g., Belušić et al., 2007) are the two main mechanisms that are known to maintain and propagate meteotsunamigenic disturbances in the atmosphere.

It should also be noted that not all high-frequency sea-level oscillations may be related to the propagation of the above described meteotsunamigenic disturbances. Indeed, extreme wind-driven wave breaking associated with atmospheric rivers (Carvajal et al., 2021) can generate strong NSLOTTs, while weak and moderate NSLOTTs can result from other atmospheric processes conjoined with specific synoptic settings that produce intrinsic variability in air pressure or wind disturbances (Uccellini and Koch, 1987).

Finally, all of the presented processes are occurring in different coastal basins and have distinct seasonal patterns (e.g., Bentley and Mote, 1998; Williams et al., 2021a), making an assessment of the global genesis of NSLOTTs rather challenging. As shown in this study in the analyses of synchronicity, it seems that zonal distributions indicate the importance of processes that favour the generation of meteotsunamigenic (and NSLOTT-genic) atmospheric disturbances over hundreds and thousands of kilometres. These processes likely include exceptionally strong mid-troposphere winds, which are usually present during extreme NSLOTT and meteotsunami events (Šepić et al., 2015a; Vilibić and Šepić, 2017). The mid-troposphere winds serve either as a proxy for the translation speed of the surface disturbances or act as a reflectance layer that allows for the ducting of atmospheric waves in the lower troposphere. Additionally, mid-tropospheric jets are sources of atmospheric gravity waves (Plougonven and Zhang, 2014), which can generate meteotsunamis. In the tropics, mid-tropospheric jets are absent, and the winds are much weaker than in the mid-latitudes (Lee, 1999); thus, no synoptic formations that favour the longevity of meteotsunamigenic disturbances (of appropriate speed equalling long ocean wave speeds) are present there. The only exceptions are hurricanes, which may also trigger meteotsunamis over wider areas (Shi et al., 2020; Lin and Wu, 2021).

5. Conclusions and perspectives

After the initial study by Vilibić and Šepić (2017), this study is a way forwards to construct global climatologies of the nonseismic sea-level oscillations at tsunami timescales (NSLOTTs). The NSLOTTs may be dominant contributors to sea-level extremes in some ocean basins, particularly in those characterised by a low tidal potential (Vilibić and Šepić, 2017). These analyses encompassed global mapping of the variance, range, spectral energy and synchronicity of the total high-frequency signal and extreme NSLOTT events. The following conclusions may be drawn from the analyses:

1. Despite the rather low variance, the range of NSLOTTs is large during extreme NSLOTT episodes and thus suggests the importance of the short-period processes during strong events.
2. The distributions of the NSLOTTs – quantified by the *Z*-score – vary zonally and between regions, indicating their connectivity either to the (i) capacity of coastal and shelf topography and bathymetry to resonantly amplify the incoming oscillations or oscillations generated at the shelf or (ii) intensity and frequency of atmospheric processes capable of generating long ocean waves.
3. The NSLOTT variance and median of the ranges reach maximum values during wintertime. However, the extreme NSLOTTs (99.99th percentile) have less pronounced seasonal patterns and may occur throughout the year, and their distributions differ at nearby stations, presumably due to local bathymetric properties. This somewhat contrasts the meteotsunami catalogues, which are mostly focused on the summer seasons, yet the methodologies between evaluating these two are different.

4. Spectral distributions of the NSLOTT periods differ among the stations, i.e., having a larger amount of energy either at lower or higher frequencies. The latter presumably depends on amplification properties of the bathymetry and coastal bathymetry, which are more efficient at higher frequencies, as the extreme NSLOTT events are generally characterised by lower spectral slopes than background NSLOTT oscillations, with higher energy amplification occurring from minutes to a few tens of minutes at maximum.
5. The NSLOTT extreme events at a station are recorded conjointly at approximately 20–32% of all surrounding stations in the mid-latitudes, possibly pointing to their connectivity through the common atmospheric synoptic patterns propagating over a region. As such patterns are presumably not present over the tropics (except hurricanes), no synchronicity has been recorded there.

High-frequency sea-level oscillations do not generally constitute a significant part of the overall sea-level oscillations. Tides, surges, seiches and other processes undoubtedly contribute more to ordinary fluctuations in sea level. However, the ability of extreme NSLOTTs to increase tenfold or even hundredfold to background NSLOTT oscillations might cause sea-level extremes and flooding, especially when combined with higher tides and storm surges, on top of the increased mean sea levels. Furthermore, NSLOTT events, even those of moderate magnitude, may generate strong rip currents and pose a threat to beaches and harbours (Linares et al., 2019). Accordingly, the assessment of extreme NSLOTT events should become the standard in coastal hazard and risk assessment studies, as already proposed by Šepić et al. (2015a) and Vilibić and Šepić (2017).

Another research avenue to explore can be the understanding and global quantification of the underlying processes contributing to NSLOTT genesis. Presently, a noteworthy level of understanding the genesis of meteotsunamis, which can be considered the most extreme NSLOTT events, has been reached, yet there are still some gaps. For example, NSLOTTs are found to peak mostly in winter but are frequently not connected with travelling air pressure and wind disturbances, contrary to the catalogued and more researched events. This opens the question about the atmospheric processes and the transfer of energy from the atmosphere towards the sea during these winter NSLOTT events, which are presumably more pronounced in the northern mid-latitudes (e.g., Baltic Sea, Pellikka et al., 2020). Convincingly, the quantification of NSLOTT genesis at the global scale is still a far-future research challenge, yet it might be bypassed by using advanced clustering or learning techniques over the known process-level variables attainable from available data and products (e.g., wave ducting can be detected from the reanalysis data, Šepić et al., 2016).

Due to the limitations of technology within earlier tide-gauge mechanisms, lower computational power of data systems and smaller data-storage capacities, historical sea-level datasets are measured at hourly (or lower) temporal resolution and, therefore, cannot be used to properly study NSLOTTs. To investigate such events, data used for analyses should be sampled with a resolution of a minute or higher. In recent decades, such technologies have been developed, allowing for new and modern approaches in tide gauge measurements. Nevertheless, a challenge of these technologies is how to keep high-quality data necessary for research, particularly in the development of automatized quality check procedures (UNESCO/IOC, 2020). There are no world data repositories for quality checked data at a minute timescale, aside from some research analysis products such as the MISELA dataset (Zemunik et al., 2021a, 2021b), which contains high-pass ($T < 2$ h) filtered minute time series. It should be highlighted here that tide gauge observations are relevant for the geosciences and that their continuity and accuracy are essential for understanding, quantifying and detecting NSLOTT phenomena (Vilibić et al., 2016). Therefore, the importance of financial and effortful investments for developing tide-gauge networks and providing research quality data at minute timescales must be emphasised. We hope and believe that the sea-level data community, in particular the providers of sea-level research quality data, will put forth effort in that direction.

Declaration of Competing Interest

The authors declare that they have no conflict of interest.

Acknowledgements

We are grateful to a hundred of data providers and thousands of researchers, engineers and technicians engaged in the maintenance of tide gauge stations whose data is included in the MISELA dataset used in our research. In line with that, we appreciate the work of Leon Ćatipović and Havu Pellikka in performing quality control of the data. Comments raised by the anonymous reviewer and the editor Liviu Matenco greatly improved the quality of the presented work. The work has been conducted through “Young Researchers' Career Development Project – Training New Doctoral Students” of the Croatian Science Foundation, with the support of the Croatian Science Foundation projects ADIOS (Grant IP-2016-06-1955) and the Horizon 2020 project SHExtreme (ERC-StG Grant 853045).

References

Abdennadher, J., Boukthir, M., 2006. Numerical simulation of the barotropic tides in the Tunisian Shelf and the Strait of Sicily. J. Mar. Syst. 63 (3–4), 162–182. https://doi.org/10.1016/j.jmarsys.2006.07.001.

Arbic, B.K., St-Laurent, P., Sutherland, G., Garrett, C., 2007. On the resonance and influence of the tides in Ungava Bay and Hudson Strait. Geophys. Res. Lett. 34, L17606. https://doi.org/10.1029/2007GL030845.

Arns, A., Wahl, T., Haigh, I.D., Jensen, J., Pattiaratchi, C., 2013. Estimating extreme water level probabilities: a comparison of the direct methods and recommendations for best practise. Coast. Eng. 81, 51–66. https://doi.org/10.1016/j.coastaleng.2013.07.003.

Bechle, A.J., Wu, C.H., Kristovich, D.A.R., Anderson, E.J., Schwab, D.J., Rabinovich, A. B., 2016. Meteotsunamis in the Laurentian Great Lakes. Sci. Rep. 6, 37832. https://doi.org/10.1038/srep37832.

Belušić, D., Grisogono, B., Klaić, Z.B., 2007. Atmospheric origin of the devastating coupled air-sea event in the east Adriatic. J. Geophys. Res. Atmos. 112, D17111. https://doi.org/10.1029/2006JD008204.

Bentley, M.L., Mote, T.L., 1998. A climatology of derecho-producing mesoscale convective systems in the Central and Eastern United States, 1986–95. Part I: temporal and spatial distribution. Bull. Am. Meteorol. Soc. 79, 2527–2540. https://doi.org/10.1175/1520-0477(1998)079<2527:ACODPM>2.0.CO;2.

Calafat, F.M., Marcos, M., 2020. Probabilistic reanalysis of storm surge extremes in Europe. Proc. Natl. Acad. Sci. U. S. A. 117, 1877–1883. https://doi.org/10.1073/pnas.1913049117.

Camelo, J., Mayo, T.L., Gutmann, E.D., 2020. Projected climate change impacts on hurricane storm surge inundation in the coastal United States. Front. Built Environ. 6, 588049 https://doi.org/10.3389/fbuil.2020.588049.

Candela, J., Mazzola, S., Sammari, C., Limeburner, R., Lozano, C.J., Patti, B., Bonnano, A., 1999. The ‘mad sea’ phenomenon in the Strait of Sicily. J. Phys. Oceanogr. 29, 2210–2231. https://doi.org/10.1175/1520-0485(1999)029<2210:TMSPIT>2.0.CO;2.

Carvajal, M., Winckler, P., Garreaud, R., Igualt, F., Contreras-López, M., Averil, P., Cisternas, M., Gubler, A., Breuer, W.A., 2021. Extreme Sea levels at Rapa Nui (Easter Island) during intense atmospheric rivers. Nat. Hazards 106, 1619–1637. https://doi.org/10.1007/s11069-020-04462-2.

Cayan, D.R., Bromirski, P.D., Hayhoe, K., Tyree, M., Dettinger, M.D., Flick, R.E., 2008. Climate change projections of sea level extremes along the California coast. Clim. Chang. 87 (S1), 57–73. https://doi.org/10.1007/s10584-007-9376-7.

Church, J.A., White, N.J., 2006. A 20th century acceleration in global sea-level rise. Geophys. Res. Lett. 33 (1), L01602. https://doi.org/10.1029/2005gl024826.

Churchill, D.D., Houston, S.H., Bond, N.A., 1995. The Daytona Beach wave of 3–4 July 1992: a shallow water gravity wave forced by a propagating squall line. Bull. Am. Meteorol. Soc. 76, 21–32. https://doi.org/10.1175/1520-0477(1995)076%3c002 1:TDBWO J%3e2.0.CO;2.

Denamiel, C., Šepić, J., Vilibić, I., 2018. Impact of geomorphological changes to harbor resonance during meteotsunamis: the Vela Luka Bay test case. Pure Appl. Geophys. 175, 3839–3859. https://doi.org/10.1007/s0002 4-018-1862-5.

Douglas, B.C., 1992. Global sea level acceleration. J. Geophys. Res. 97 (C8), 12699. https://doi.org/10.1029/92jc01133.

Dusek, G., DiVeglio, C., Licate, L., Heilman, L., Kirk, K., Paternostro, C., Miller, A., 2019. A meteotsunami climatology along the U.S. East Coast. Bull. Am. Meteorol. Soc. 100 (7), 1329–1345. https://doi.org/10.1175/BAMS-D-18-0206.1.

Ewing, M., Press, F., Donn, W.L., 1954. An explanation of the Lake Michigan wave of 26 June 1954. Science 120 (3122), 684–686. https://doi.org/10.1126/science.120.3122.684.

Farnbach, J.S., 1975. The complex envelope in seismic signal analysis. Bull. Seismol. Soc. Am. 65, 951–962. https://doi.org/10.1785/BSSA0650040951.
Gomis, D., Monserrat, S., Tintoré, J., 1993. Pressure-forced seiches of large amplitude in inlets of the Balearic Islands. J. Geophys. Res. 98, 14437–14445. https://doi.org/10.1029/93JC00623.
Goring, D.G., 2009. Meteotsunami resulting from the propagation of synoptic-scale weather systems. Phys. Chem. Earth 34 (17–18), 1009–1015. https://doi.org/10.1016/j.pce.2009.10.004.
Greenspan, H.P., 1956. The generation of edge waves by moving pressure disturbances. J. Fluid Mech. 1, 574–592.
Gusiakov, V.K., 2021. Meteotsunamis at global scale: problems of event identification, parameterization and cataloguing. Nat. Hazards 106, 1105–1123. https://doi.org/10.1007/s11069-020-04230-2.
Haigh, I.D., Pickering, M.D., Green, J.A.M., Arbic, B.K., Arns, A., Dangendorf, S., Hill, D. F., Horsburgh, K., Howard, T., Idier, D., Jay, D.A., Jänicke, L., Lee, S.B., Müller, M., Schindelegger, M., Talke, S.A., Wilmes, S.-B., Woodworth, P.L., 2019. The tides they are a-changin': A comprehensive review of past and future nonastronomical changes in tides, their driving mechanisms and future implications. Rev. Geophys. 57, e2018RG000636 https://doi.org/10.1029/2018RG000636.
Hartmann, D.L., 2007. The atmospheric general circulation and its variability. J. Meteorol. Soc. Jpn. Ser. II. 85B (0), 123–143. https://doi.org/10.2151/jmsj.85B.123.
Heidarzadeh, M., Rabinovich, A.B., 2021. Combined hazard of typhoon-generated meteorological tsunamis and storm surges along the coast of Japan. Nat. Hazards 106, 1639–1672. https://doi.org/10.1007/s11069-020-04448-0.
Hibiya, T., Kajiura, K., 1982. Origin of the Abiki phenomenon (a kind of seiche) in Nagasaki Bay. J. Oceanogr. Soc. Jpn 38 (3), 172–182. https://doi.org/10.1007/bf02110288.
Hill, D.F., 2016. Spatial and temporal variability in tidal range: evidence, causes, and effects. Curr. Clim. Change Rep. 2 (4), 232–241. https://doi.org/10.1007/s40641-016-0044-8.
Hunter, J., 2010. Estimating sea-level extremes under conditions of uncertain sea-level rise. Clim. Chang. 99 (3–4), 331–350. https://doi.org/10.1007/s10584-009-9671-6.
Hunter, J.R., Woodworth, P.L., Wahl, T., Nicholls, R.J., 2017. Using global tide gauge data to validate and improve the representation of extreme sea levels in flood impact studies. Glob. Planet. Chang. 156, 34–45. https://doi.org/10.1016/j.gloplacha.2017.06.007.
Hurt-Davis, M.G., Piccioni, G., Dettmering, D., Schwatke, C., Passaro, M., Seitz, F., 2021. EOT20: a global ocean tide model from multi-mission satellite altimetry. Earth Syst. Sci. Data 13, 3869–3884. https://doi.org/10.5194/essd-13-3869-2021.
Jansà, A., Ramis, C., 2021. The Balearic rissaga: from pioneering research to present-day knowledge. Nat. Hazards 106, 1269–1297. https://doi.org/10.1007/s11069-020-04221-3.
Jansa, A., Monserrat, S., Gomis, D., 2007. The rissaga of 15 June 2006 in Ciutadella (Menorca), a meteorological tsunami. Adv. Geosci. 12, 1–4. https://doi.org/10.5194/adgeo-12-1-2007.
Johns, R.H., Hirt, W.D., 1987. Derechos: Widespread convectively induced windstorms. Weather Forecast. 2, 32–49. https://doi.org/10.1175/1520-0434(1987)002<0032:DWCIW>2.0.CO;2.
de Jong, M.P.C., Battjes, J.A., 2004. Low-frequency Sea waves generated by atmospheric convection cells. J. Geophys. Res. Oceans 109, C01011. https://doi.org/10.1029/2003JC001931.
de Jong, M.P.C., Holthuijsen, L.H., Battjes, J.A., 2003. Generation of seiches by cold fronts over the southern North Sea. J. Geophys. Res. Oceans 108, 3117. https://doi.org/10.1029/2002JC001422.
Kazeminezhad, M.H., Vilibić, I., Denamiel, C., Ghafarian, P., Negah, S., 2021. Weather radar and ancillary observations of the convective system causing the northern Persian Gulf meteotsunami on 19 March 2017. Nat. Hazards 106, 1747–1769. https://doi.org/10.1007/s11069-020-04208-0.
Kim, J., Omira, R., 2021. The 6–7 July 2010 meteotsunami along the coast of Portugal: insights from data analysis and numerical modelling. Nat. Hazards 106, 1397–1419. https://doi.org/10.1007/s11069-020-04335-8.
Kim, M.-S., Woo, S.-B., Eom, H., You, S.H., 2021. Occurrence of pressure-forced meteotsunami events in the eastern Yellow Sea during 2010–2019. Nat. Hazards Earth Syst. Sci. 21, 3323–3337. https://doi.org/10.5194/nhess-21-3323-2021.
Lee, S., 1999. Why are the climatological zonal winds easterly in the equatorial upper troposphere? J. Atmos. Sci. 56, 1353–1363. https://doi.org/10.1175/1520-0469(1999)056<1353:WATCZW>2.0.CO;2.
Leys, C., Ley, C., Klein, O., Bernard, P., Licata, L., 2013. Detecting outliers: do not use standard deviation around the mean, use absolute deviation around the median. J. Exp. Soc. Psychol. 49, 764–766. https://doi.org/10.1016/j.jesp.2013.03.013.
Lin, L.-C., Wu, C.H., 2021. Unexpected meteotsunamis prior to Typhoon Wipha and Typhoon Neoguri. Nat. Hazards 106, 1673–1686. https://doi.org/10.1007/s11069-020-04313-0.
Linares, Á., Wu, C.H., Bechle, A.J., Anderson, E.J., Kristovich, D.A.R., 2019. Unexpected rip currents induced by a meteotsunami. Sci. Rep. 9 (1), 2105. https://doi.org/10.1038/s41598-019-38716-2.
Marcos, M., Monserrat, S., Medina, R., Orfila, A., Olabarrieta, M., 2009. External forcing of meteorological tsunamis at the coast of the Balearic Islands. Phys. Chem. Earth 34, 938–947. https://doi.org/10.1016/j.pce.2009.10.001.
Medvedev, I.P., Vilibić, I., Rabinovich, A.B., 2020. Tidal resonance in the Adriatic Sea: observational evidence. J. Geophys. Res. Oceans 125 (8), e2020JC016168. https://doi.org/10.1029/2020jc016168.
Melet, A., Almar, R., Hemer, M., Le Cozannet, G., Meyssignac, B., Ruggiero, P., 2020. Contribution of wave setup to projected coastal sea level changes. J. Geophys. Res. Oceans 125, e2020JC016078. https://doi.org/10.1029/2020JC016078.
Merrifield, M.A., Becker, J.M., Ford, M., Yao, Y., 2014. Observations and estimates of wave-driven water level extremes at the Marshall Islands. Geophys. Res. Lett. 41, 7245–7253. https://doi.org/10.1002/2014GL061005.
Miles, J., Munk, W., 1961. Harbor paradox. J. Waterw. Harbor Div. ASCE 87, 111–132.
Monserrat, S., Thorpe, A.J., 1996. Use of ducting theory in an observed case of gravity waves. J. Atmos. Sci. 53, 1724–1736. https://doi.org/10.1175/1520-0469(1996)053<1724:UODTIA>2.0.CO;2.
Monserrat, S., Ibberson, A., Thorpe, A.J., 1991. Atmospheric gravity waves and the "rissaga" phenomenon. Q. J. R. Meteorol. Soc. 117, 553–570. https://doi.org/10.1002/qj.49711749907.
Monserrat, S., Rabinovich, A.B., Casas, B., 1998. On the reconstruction of the transfer function for atmospherically generated seiches. Geophys. Res. Lett. 25, 2197–2200. https://doi.org/10.1029/98GL0 1506.
Monserrat, S., Vilibić, I., Rabinovich, A.B., 2006. Meteotsunamis: atmospherically induced destructive ocean waves in the tsunami frequency band. Nat. Hazard Earth Sys. 6 (6), 1035–1051. https://doi.org/10.5194/nhess-6-1035-2006.
Muis, S., Apecechea, M.I., Dullaart, J., de Lima Rego, J., Skovgaard Madsen, K., Su, J., Yan, K., Verlaan, M., 2020. A high-resolution global dataset of extreme sea levels, tides, and storm surges, including future projections. Front. Mar. Sci. 7, 263. https://doi.org/10.3389/fmars.2020.00263.
Neale, J., Harmon, N., Srokosz, M., 2015. Source regions and reflection of infragravity waves offshore of the U.S.s Pacific Northwest. J. Geophys. Res. Oceans 120, 6474–6491. https://doi.org/10.1002/2015JC010891.
Neumann, B., Vafeidis, A.T., Zimmermann, J., Nicholls, R.J., 2015. Future coastal population growth and exposure to sea-level rise and coastal flooding—a global assessment. PLoS One 10 (3), e0118571. https://doi.org/10.1371/journal.pone.0118571.
Nicholls, R.J., 2011. Planning for the impacts of sea level rise. Oceanography 24 (2), 144–157. https://doi.org/10.5670/oceanog.2011.34.
Odamaki, M., 1989. Co-oscillating and independent tides of the Japan Sea. J. Oceanogr. Soc. Jpn 45, 217–232. https://doi.org/10.1007/BF02123465.
Orlić, M., 1980. About a possible occurrence of the Proudman resonance in the Adriatic. Thalass. Jugosl. 16, 79–88.
Orlić, M., 2015. The first attempt at cataloguing tsunami-like waves of meteorological origin in Croatian coastal waters. Acta Adriat. 56 (1), 83–96.
Orlić, M., Belušić, D., Janeković, I., Pasarić, M., 2010. Fresh evidence relating the great Adriatic surge of 21 June 1978 to mesoscale atmospheric forcing. J. Geophys. Res. 115, C06011. https://doi.org/10.1029/2009JC005777.
Ozsoy, O., Haigh, I.D., Wadey, M.P., Nicholls, R.J., Wells, N.C., 2016. High-frequency Sea level variations and implications for coastal flooding: a case study of the Solent, UK. Cont. Shelf Res. 122, 1–13. https://doi.org/10.1016/j.csr.2016.03.021.
Pasquet, S., Vilibić, I., Šepić, J., 2013. A survey of strong high-frequency sea level oscillations along the U.S. East Coast between 2006 and 2011. Nat. Hazards Earth Syst. Sci. 13, 473–482. https://doi.org/10.5194/nhess-13-473-2013.
Pattiaratchi, C., Wijeratne, E.M.S., 2014. Observations of meteorological tsunamis along the south-west Australian coast. Nat. Hazards 74 (1), 281–303. https://doi.org/10.1007/s11069-014-1263-8.
Pattiaratchi, C., Wijeratne, E.M.S., 2015. Are meteotsunamis an underrated hazard? Phil. Trans. R. Soc. A 373, 20140377. https://doi.org/10.1098/rsta.2014.0377.
Pawlowicz, R., Beardsley, B., Lentz, S., 2002. Classical tidal harmonic analysis including error estimates in MATLAB using T_TIDE. Comput. Geosci. 28, 929–937. https://doi.org/10.1016/S0098-3004(02)00013-4.
Pellikka, H., Laurila, T.K., Boman, H., Karjalainen, A., Björkqvist, J.-V., Kahma, K.K., 2020. Meteotsunami occurrence in the Gulf of Finland over the past century. Nat. Hazards Earth Syst. Sci. 20, 2535–2546. https://doi.org/10.5194/nhess-20-2535-2020.
Plougonven, R., Zhang, F., 2014. Internal gravity waves from atmospheric jets and fronts. Rev. Geophys. 52, 33–76. https://doi.org/10.1002/2012RG000419.
Proudman, J., 1929. The effects on the sea of changes in atmospheric pressure. Geophys. J. Int. 2, 197–209. https://doi.org/10.1111/j.1365-246X.1929.tb05408.x.
Rabinovich, A.B., 2009. Seiches and harbour oscillations. In: Kim, Y.C. (Ed.), Handbook of Coastal and Ocean Engineering. World Scientific, Singapore, pp. 193–236. https://doi.org/10.1142/97898 12819307_0009.
Rabinovich, A.B., 2020. Twenty-seven years of progress in the science of meteorological tsunamis following the 1992 Daytona Beach event. Pure Appl. Geophys. 177, 1193–1230. https://doi.org/10.1007/s00024-019-02349-3.
Raichlen, F., 1966. Harbor resonance. In: Ippen, A.T. (Ed.), Estuary and Coastline Hydrodynamics. McGraw Hill Book Comp, New York, pp. 281–340.
Rawat, A., Ardhuin, F., Ballu, V., Crawford, W., Corela, C., Aucan, J., 2014. Infragravity waves across the oceans. Geophys. Res. Lett. 41, 7957–7963. https://doi.org/10.1002/2014GL061604.
Šepić, J., Rabinovich, A.B., 2014. Meteotsunami in the Great Lakes and on the Atlantic coast of the United States generated by the "derecho" of June 29–30, 2012. Nat. Hazards 74, 75–107. https://doi.org/10.1007/s1106 9-014-1310-5.
Šepić, J., Vilibić, I., Monserrat, S., 2009. Teleconnections between the Adriatic and the Balearic meteotsunamis. Phys. Chem. Earth 34, 928–937. https://doi.org/10.1016/j.pce.2009.08.007.
Šepić, J., Vilibić, I., Lafon, A., Macheboeuf, L., Ivanović, Z., 2015a. High-frequency Sea level oscillations in the Mediterranean and their connection to synoptic patterns. Prog. Oceanogr. 137, 284–298. https://doi.org/10.1016/j.pocean.2015.07.005.
Šepić, J., Vilibić, I., Rabinovich, A.B., Monserrat, S., 2015b. Widespread tsunami-like waves of 23-27 June in the Mediterranean and Black Seas generated by high-altitude atmospheric forcing. Sci. Rep. 5 (1), 11682. https://doi.org/10.1038/srep11682.
Šepić, J., Vilibić, I., Monserrat, S., 2016. Quantifying the probability of meteotsunami occurrence from synoptic atmospheric patterns. Geophys. Res. Lett. 43, 10377–10384. https://doi.org/10.1002/2016GL070754.

Shao, D., Xing, Y., Zheng, Z.R., Jiang, G., 2020. Investigation of harbor oscillations originated from the vessel-induced bores using methods of autoregressive model and Mahalanobis distance. Ocean Eng. 207, 107385 https://doi.org/10.1016/j.oceaneng.2020.107385.

Shi, L.M., Olabarrieta, M., Nolan, D.S., Warner, J.C., 2020. Tropical cyclone rainbands can trigger meteotsunamis. Nat. Commun. 11, 678. https://doi.org/10.1038/s41467-020-14423-9.

Sibley, A.M., Cox, D., Tappin, D.R., 2021. Convective rear-flank downdraft as driver for meteotsunami along English Channel and North Sea coasts 28–29 May 2017. Nat. Hazards 106, 1445–1465. https://doi.org/10.1007/s11069-020-04328-7.

Sun, A.Y., Scanton, B.R., 2019. How can Big Data and machine learning benefit environment and water management: a survey of methods, applications, and future directions. Environ. Res. Lett. 14, 073001 https://doi.org/10.1088/1748-9326/ab1b7d.

Thomson, R.E., Emery, W.J., 2014. Data Analysis Methods in Physical Oceanography. Third and revised edition. Elsevier Science, Amsterdam, London, New York.

Thotagamuwage, D.T., Pattiaratchi, C.B., 2014. Influence of offshore topography on infragravity period oscillations in Two Rocks Marina, Western Australia. Coast. Eng. 91, 220–230. https://doi.org/10.1016/j.coastaleng.2014.05.011.

Titov, V., Rabinovich, A.B., Mofjeld, H.O., Thomson, R.E., González, F.I., 2005. The global reach of the 26 December 2004 Sumatra tsunami. Science 309 (5743), 2045–2048. https://doi.org/10.1126/science.1114576.

Tsimplis, M.N., Proctor, R., Flather, R.A., 1995. A two-dimensional tidal model for the Mediterranean Sea. J. Geophys. Res. 100, 16223–16239. https://doi.org/10.1029/95JC01671.

Tsimplis, M.N., Marcos, M., Pérez, B., Challenor, P., Garcia-Fernandez, M.J., Raicich, F., 2009. On the effect to the sampling frequency of sea level measurements on return period estimate of extremes – Southern European examples. Cont. Shelf Res. 29, 2214–2221. https://doi.org/10.1016/j.csr.2009.08.015.

Uccellini, L.W., Koch, S.E., 1987. The synoptic setting and possible energy sources for mesoscale wave disturbances. Mon. Weather Rev. 115, 721–729. https://doi.org/10.1175/1520-0493(1987)115<0721:TSSAPE>2.0.CO;2.

Ulbrich, U., Leckebusch, G.C., Pinto, J.G., 2009. Extra-tropical cyclones in the present and future climate: a review. Theor. Appl. Clim. 96, 117–131. https://doi.org/10.1007/s00704-008-0083-8.

UNESCO/IOC, 2020. Quality Control of in situ Sea Level Observations: A Review and Progress towards Automated Quality Control, Vol. 1. UNESCO, Paris (IOC Manuals and Guides No. 83, 44 pp.).

Vilibić, I., Šepić, J., 2009. Destructive meteotsunamis along the eastern Adriatic coast: overview. Phys. Chem. Earth 34, 904–917. https://doi.org/10.1016/j.pce.2009.08.004.

Vilibić, I., Šepić, J., 2017. Global mapping of nonseismic sea level oscillations at tsunami timescales. Sci. Rep. 7, 40818. https://doi.org/10.1038/srep40818.

Vilibić, I., Šepić, J., Rabinovich, A.B., Monserrat, S., 2016. Modern approaches in meteotsunami research and early warning. Front. Mar. Sci. 3, 57. https://doi.org/10.3389/fmars.2016.00057.

Vilibić, I., Denamiel, C., Zemunik, P., Monserrat, S., 2021a. The Mediterranean and Black Sea meteotsunamis: an overview. Nat. Hazards 106, 1223–1267. https://doi.org/10.1007/s11069-020-04306-z.

Vilibić, I., Rabinovich, A.B., Anderson, E.J., 2021b. Special issue on the global perspective on meteotsunami science: editorial. Nat. Hazards 106, 1087–1104. https://doi.org/10.1007/s11069-021-04679-9.

Vousdoukas, M.I., Mentaschi, L., Voukouvalas, E., Verlaan, M., Jevrejeva, S., Jackson, L.P., Feyen, L., 2018. Global probabilistic projections of extreme sea levels show intensification of coastal flood hazard. Nat. Commun. 9 (1), 2360. https://doi.org/10.1038/s41467-018-04692-w.

Webb, S.C., Zhang, X., Crawford, W., 1991. Infragravity waves in the deep ocean. J. Geophys. Res. Oceans 96, 2723–2736. https://doi.org/10.1029/90JC02212.

Williams, D.A., Horsburgh, K.J., Schultz, D.M., Hughes, C.W., 2019b. Examination of generation mechanisms for an English Channel meteotsunami: combining observations and modeling. J. Phys. Oceanogr. 49, 103–120. https://doi.org/10.1175/JPO-D-18-0161.1.

Williams, D.A., Schultz, D.M., Horsburgh, K.J., Hughes, C.W., 2021a. An 8-yr meteotsunami climatology across Northwest Europe: 2010–17. J. Phys. Oceanogr. 1145–1161 https://doi.org/10.1175/JPO-D-20-0175.1.

Williams, D.A., Horsburgh, K.J., Schultz, D.M., Hughes, C.W., 2021b. Proudman resonance with tides, bathymetry and variable atmospheric forcings. Nat. Hazards 106, 1169–1194. https://doi.org/10.1007/s11069-020-03896-y.

Williams, J., Matthews, A., Jevrejeva, S., 2019a. Development of an automatic tide gauge processing system. In: National Oceanography Centre Research and Consultancy Report, 64. National Oceanography Centre, Southampton (26 pp.).

Woodworth, P.L., 2017. Seiches in the Eastern Caribbean. Pure Appl. Geophys. 174, 4283–4312. https://doi.org/10.1007/s00024-017-1715-7.

Woodworth, P.L., Aman, A., Aarup, T., 2007. Sea level monitoring in Africa. Afr. J. Mar. Sci. 29, 321–330. https://doi.org/10.2989/AJMS.2007.29.3.2.332.

Woodworth, P.L., Menendez, M., Gehrels, W.R., 2011. Evidence for century-timescale acceleration in mean sea levels and for recent changes in extreme sea levels. Surv. Geophys. 32 (4–5), 603–618. https://doi.org/10.1007/s10712-011-9112-8.

Woodworth, P.L., Hunter, J.R., Marcos Moreno, M., Caldwell, P.C., Menendez, M., Haigh, I.D., 2016. GESLA (Global Extreme Sea Level Analysis) High Frequency Sea Level Dataset - Version 2. British Oceanographic Data Centre - Natural Environment Research Council, UK (doi:10/bp74).

Woodworth, P.L., Hunter, J.R., Marcos, M., Caldwell, P., Menéndez, M., Haigh, I., 2017. Towards a global higher-frequency sea level dataset. Geosci. Data J. 3 (2), 50–59. https://doi.org/10.1002/gdj3.42.

Zemunik, P., Vilibić, I., Šepić, J., Pellikka, H., Ćatipović, L., 2021a. MISELA: Minute Sea-Level Analysis. Marine Data Archive. https://doi.org/10.14284/456.

Zemunik, P., Vilibić, I., Šepić, J., Pellikka, H., Ćatipović, L., 2021b. MISELA: 1-minute sea-level analysis global dataset. Earth Syst. Sci. Data 13, 4121–4132. https://doi.org/10.5194/essd-13-4121-2021.

Zemunik, P., Bonanno, A., Mazzola, S., Giacalone, G., Fontana, I., Genovese, S., Basilone, G., Candela, J., Šepić, J., Vilibić, I., Aronica, S., 2021c. Observing meteotsunamis ("Marrobbio") on the southwestern coast of Sicily. Nat. Hazards 106, 1337–1363. https://doi.org/10.1007/s11069-020-04303-2.